

From Geostrophic to Magnetically-Damped Turbulence in Liquid Metal Rotating Magnetoconvection

Tao Liu^a, Yufan Xu^b, Jewel A. Abbate^a, Jonathan S. Cheng^c, Jonathan M. Aurnou^a

^a*Earth, Planetary, and Space Sciences, University of California, Los Angeles, CA, USA*

^b*Princeton Plasma Physics Laboratory, Princeton, NJ, USA*

^c*Mechanical and Nuclear Engineering, United States Naval Academy, Annapolis, MD, USA*

Abstract

Understanding planetary core convection dynamics requires the study of convective flows in which the Coriolis and Lorentz forces attain a leading-order, so-called magnetostrophic balance. Experimental investigations of rotating magnetoconvection (RMC) in the magnetostrophic regime are therefore essential to broadly characterize the properties of local-scale planetary core flow. Towards this end, we present here the first thermovelocimetric measurements of magnetostrophic, liquid metal convection, which are made using liquid gallium as the working fluid, at moderate rotation rates (Ekman numbers $10^{-4} \leq Ek \leq 10^{-5}$) and in the presence of dynamically strong magnetic fields (Elsasser number $\Lambda = 1$). Complementary rotating convection (RC) experiments are performed at the same rotation rates to serve as reference cases. Our RMC velocity measurements adequately follow a geostrophic turbulent scaling for cases in which local-scale convective inertial forces exceed the Lorentz forces in the fluid bulk. In cases where Lorentz forces exceed local-scale inertia ($N_\ell \gtrsim 3$), the root-mean-square RMC velocities are magnetically damped, yielding values below the geostrophic turbulent RC scaling prediction. An enhancement in heat transfer is observed, which we attribute to the increased coherence of vertically aligned magnetostrophic convective flow. Extrapolating these laboratory results, we predict that convection-scale flows in Earth's core occur in the magnetically damped $N_\ell \gtrsim 3$ regime with Rayleigh number values between 10^{24} and 10^{26} .

Keywords: Core dynamics, Magnetostrophy, Convective turbulence

1. Introduction

Earth’s outer core dynamics are primarily governed by convective turbulent flows of molten iron and nickel, which sustain the geodynamo process responsible for generating the planet’s magnetic field (Roberts and King, 2013). These complex fluid motions are driven by buoyancy-induced convection, influenced by rapid rotation and electromagnetic forces within the liquid outer core (Jones, 2011). Under the influence of the Coriolis effect induced by Earth’s rapid rotation, outer core flows tend to organize into anisotropic, columnar modes that are elongated parallel to the rotation axis, a phenomenon known as the Proudman–Taylor (P-T) constraint (Proudman and Lamb, 1916; Taylor and Lamb, 1917; Greenspan, 1969). However, linear theory suggests that when the Coriolis and Lorentz forces reach a leading-order “magnetostrophic” balance, the P-T constraint is relaxed. It has long been postulated that this magnetostrophic relaxation allows planetary core convection to develop into an optimal state, facilitating more efficient heat and compositional transport within the outer core (Chandrasekhar and Elbert, 1955; Eltayeb and Chandrasekhar, 1972; King and Aurnou, 2015; Yadav et al., 2016a; Horn and Aurnou, 2025). However, few studies have characterized the properties of magnetostrophic convective flow. Thus, the properties of magnetostrophic convection are not well known. Further, it is not known if magnetostrophic convection is indeed optimal for generating dynamo action in planetary core settings.

Our cylindrical laboratory experiments simulate a local fluid parcel within Earth’s outer core to investigate small-scale convection dynamics in electrically conducting liquid metals, as shown schematically in Figure 1a. Previous experimental studies using liquid gallium have revealed evidence of magnetostrophic convective flow by demonstrating enhanced heat transfer at Elsasser number $\Lambda \sim 1$ (King and Aurnou, 2015). However, laboratory velocity measurements of the “optimized” flow field claimed to develop in the magnetostrophic regime are still lacking. In this study, we employ the ‘RoMag’ apparatus at UCLA, filled with liquid gallium and capable of imposing both Coriolis and Lorentz forces to explore magnetostrophic dynamics in greater detail. In particular, we quantify the thermally driven flow velocities that arise in the magnetostrophic RMC regime.

Numerical simulations in spherical shell geometries suggest that the presence of magnetic fields can enhance convective efficiency, especially in polar regions of rotating spherical shells (Yadav et al., 2016a). Further, Yadav et al.

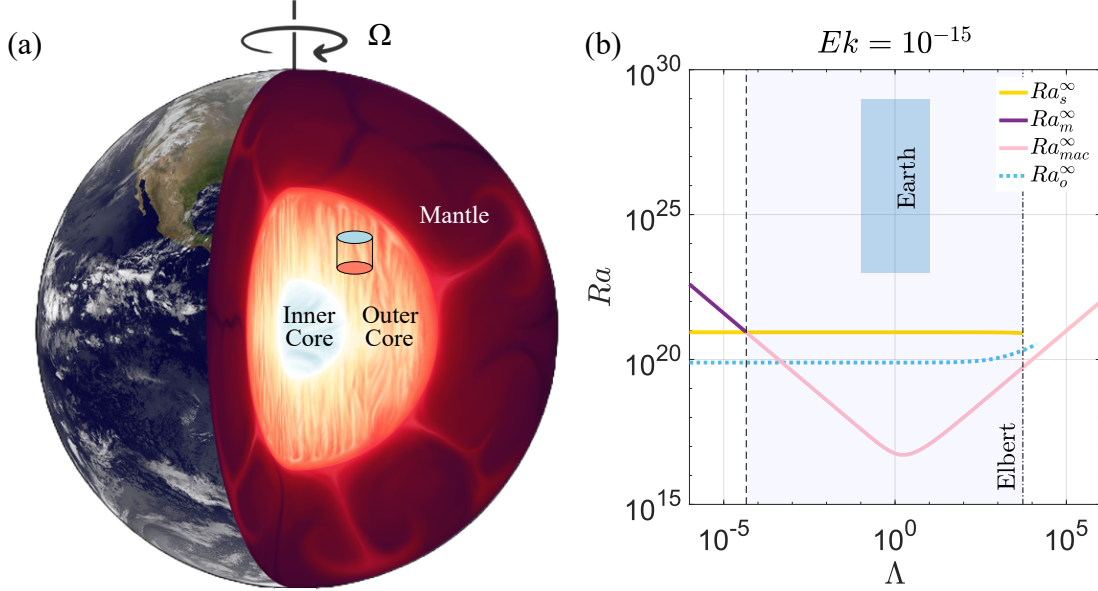


Figure 1: (a) Illustration of earth interior with a cylindrical container in outer core representing the simulated laboratory setup (Earth surface image: NASA/NOAA/GOES); (b) linear theory predictions of multi-modal rotating magnetoconvection for Earth's outer core in $Pr = 0.1$ core-like fluid, semi-transparent blue shaded rectangle shows the Ra - Λ range estimates for Earth's outer core from previous work (e.g., Gubbins, 2001).

(2016b) found a leading order geostrophic force balance in a suite of dynamo models. However, they showed that a second order magnetostrophic balance could arise on the local convective scale with the resulting flow self-organizing into slightly larger-scale, axially-aligned structures, in basic agreement with the theoretical arguments of Calkins et al. (2015) and Aurnou and King (2017).

In this work, we focus on velocity measurements in rotating magnetoconvection (RMC) over the Ekman number range $Ek \in [10^{-4}, 10^{-5}]$ at the Elsasser number $\Lambda = 1$, where Ek describes the nondimensional rotation period and Λ estimates the ratio of quasistatic Lorentz and Coriolis forces (Horn and Aurnou, 2025). Rotating convection (RC) experiments are also conducted for comparison. The measured velocities are evaluated with respect to theoretical predictions for rotating convective turbulence, including the inviscid Coriolis–Inertial–Archimedean (CIA) balance (Jones, 2011) as well as the fully diffusivity-free (DF) scaling regime (Julien et al., 2012a; Ab-

bate, 2024; Abbate et al., 2024). The interaction parameter is also calculated to quantify the ratio of Lorentz to inertial forces. It serves as an indicator of the flow regime: a high value suggests Lorentz-force dominance characteristic of the magnetostrophic regime, while a low value indicates inertial dominance, more typical of geostrophic turbulence.

This paper is organized as follows. Section 2 introduces the key dimensionless parameters and summarizes the theoretical predictions and scaling laws for rotating convection and rotating magnetoconvection. Section 3 describes the experimental setup, measurement techniques, and explored parameter space. We present and analyze the experimental results in Section 4, including transport scalings for both rotating convection and rotating magnetoconvection. In sections 5 and 6, we extrapolate our laboratory findings to Earth’s outer core conditions and summarize our findings.

2. Nondimensional parameters and theoretical background

2.1. Nondimensional parameters

Rotating convection (RC) is governed by four nondimensional parameters (Horn and Schmid, 2017; Kunnen, 2021). The Rayleigh number Ra quantifies the effect of the competition between buoyancy and diffusive effects:

$$Ra = \frac{\alpha g \Delta T H^3}{\nu \kappa}, \quad (1)$$

where α is the thermal expansion coefficient; g is gravitational acceleration; ΔT is the mean temperature difference across the fluid layer of depth H ; and ν and κ are the kinematic viscosity and the thermal diffusivity, respectively. The Ekman number Ek characterizes the relative influence of viscous forces to Coriolis forces

$$Ek = \frac{\nu}{2\Omega H^2}, \quad (2)$$

where Ω is the angular rotation rate of the system. The Prandtl number characterizes the thermomechanical properties of the material by expressing the ratio of momentum diffusivity to thermal diffusivity:

$$Pr = \frac{\nu}{\kappa}. \quad (3)$$

In addition, the geometrical aspect ratio of the cylindrical container,

$$\Gamma = \frac{D}{H}, \quad (4)$$

can play an important role in determining the convective flow structures and statistics (e.g., Weiss and Ahlers, 2011; Cheng et al., 2018; Horn et al., 2022; Xu et al., 2025). Here, R is the radius and $D = 2R$ is the diameter of the cylinder.

A fifth nondimensional parameter is needed to describe RMC systems. In local-scale core dynamics, the Elsasser number, Λ , is typically used, as it measures the relative strength of the (quasi-static) Lorentz force to the Coriolis force (Soderlund et al., 2015; Dormy, 2016; Aurnou and King, 2017; Horn and Aurnou, 2025; Teed and Dormy, 2025):

$$\Lambda = \frac{\sigma B^2}{2\rho\Omega} = Ek Ch, \quad (5)$$

where σ is the electrical conductivity of the fluid, B is the magnetic field strength, and ρ is the density of the fluid. Alternatively, one may use the Chandrasekhar number, $Ch = \sigma B^2 H^2 / (\rho\nu)$, which estimates the ratio of the Lorentz and viscous forces.

Another essential parameter is the convective Rossby number, which provides an *a priori* estimate of the ratio of the buoyancy-driven inertial and Coriolis forces acting on the local convective scale (Aurnou et al., 2020):

$$Ro_c = \sqrt{\frac{g\alpha\Delta T}{4\Omega^2 H}} = \sqrt{\frac{RaEk^2}{Pr}}. \quad (6)$$

The convective Rossby number is often used to distinguish different convective flow regimes in rotating convection (RC) systems (e.g., Gastine et al., 2013a,b; Mabuchi et al., 2015; Camisassa and Featherstone, 2022; Soderlund et al., 2025). It also scales the ratio of rapidly rotating convective flow velocities, $U_\Omega \approx \alpha g \Delta T / (2\Omega)$, and non-rotating convective velocities, $U_{ff} \approx \sqrt{\alpha g \Delta T H}$, such that $Ro_c \sim U_\Omega / U_{ff} = Re_\Omega / Re_{ff}$ (Aurnou et al., 2020). Here, $Re = UH/\nu$ is the Reynolds number, which estimates the system-scale ratio of inertial and viscous forces; the geostrophic turbulent scaling gives $Re_\Omega \sim RaEk/Pr$; and the non-rotating free-fall scaling is $Re_{ff} \sim \sqrt{Ra/Pr}$. In addition, it estimates the characteristic scale, ℓ , of geostrophic turbulent RC flows such that $\ell \approx Ro_c H$ (e.g., Abbate and Aurnou, 2024; Hadjerci et al., 2024).

The local ratio of the Lorentz and inertial forces is given by N_ℓ , the local interaction parameter,

$$N_\ell = \frac{\sigma B^2 \ell}{\rho U}. \quad (7)$$

If we assume that the convection exists in, or relatively near, the geostrophic turbulence regime, then we may take $\ell \approx Ro_c H$ and $U \approx U_\Omega$. Subbing these into (7) yields what we will call the convective interaction parameter,

$$N_c = \frac{\sigma B^2 (Ro_c H)}{\rho U_\Omega} = \frac{Ch Ro_c}{Re_\Omega}, \quad (8)$$

which can be reformulated in a variety of forms, including

$$N_c = \frac{Ch}{Re_{ff}} = \sqrt{\frac{Ch^2 Pr}{Ra}} \quad \text{and} \quad N_c = \frac{\Lambda}{Ro_c}.$$

The similarity in structure and high degree of interconnectivity between $Ro_c = \sqrt{Ra Ek^2 / Pr}$ and $N_c^{-1} = \sqrt{Ra Ch^{-2} / Pr}$ arise here because we are using the quasi-static form of the Lorentz force density $f_L \sim \sigma U B^2$, as applies in laboratory experiments (Horn and Aurnou, 2025), and also because we are choosing geostrophic turbulence estimates for the characteristic scales of ℓ and U . In contrast, the interaction parameter is not nearly so similar in structure to $1/Ro_c$ in the ageostrophic, non-quasistatic dynamo modeling study of Soderlund et al. (2025).

2.2. Convection Modes

In rotating convection in a cylinder, convection can occur via three modes of instability: oscillatory thermal-inertial, steady geostrophic, and sidewall-attached modes. We briefly introduce here the theoretical predictions for the onset and the frequency of each mode.

The oscillatory bulk mode typically dominates near onset in low-Prandtl-number fluids and is characterized by time-periodic, columnar flows spanning the fluid layer (Chandrasekhar, 1961; Julien and Knobloch, 1998; Julien et al., 1999; Zhang and Liao, 2009; Vogt et al., 2021a; Abbate et al., 2024; Xu et al., 2025). The presence of a cylindrical tank’s vertical sidewall acts to stabilize the oscillatory bulk mode, thus raising the critical Rayleigh number Ra_o^{cyl} for low Pr oscillatory modes in a cylinder (Liao et al., 2006; Zhang and Liao, 2009).

The other bulk RC mode is the steady “geostrophic” mode (Niiler and Bisshopp, 1965; Julien and Knobloch, 1998; Kunnen, 2021). It is stationary and emerges at higher Rayleigh numbers than the oscillatory modes in low Pr RC (Horn and Schmid, 2017; Aurnou et al., 2018; Vogt et al., 2021a).

Convection mode	Critical Rayleigh number	Mode frequency
Oscillatory bulk mode	$Ra_o^\infty = 17.4 (Ek/Pr)^{-4/3}$	$f_o^\infty = 4.8 (Ek/Pr)^{1/3}$
Steady geostrophic mode	$Ra_s^\infty = (8.68 - 9.63Ek^{1/6})Ek^{-4/3}$	–
Wall mode	$Ra_w = 31.8Ek^{-1} + 46.6Ek^{-2/3}$	$f_w = 131.8Ek/Pr - 1464.5Ek^{4/3}/Pr$
Steady magnetostrophic mode	$Ra_{mac}^\infty = \left(\pi^2(1 + \sqrt{1 + \Lambda^2})^2/\Lambda\right)Ek^{-1}$	–

Table 1: Critical Rayleigh number and nondimensional frequency (nondimensionalized by rotation rate) of oscillatory bulk mode, steady geostrophic mode and wall mode (Horn and Schmid, 2017) in rotating convection, and steady magnetostrophic mode in rotating magnetoconvection (Horn and Aurnou, 2022). The superscript ∞ denotes values in an infinite layer.

The transition from the conductive sidewall state to an asymmetric traveling-wave state occurs via a supercritical Hopf bifurcation for all Pr fluids (e.g., Zhong et al., 1991; Goldstein et al., 1994; Vasil et al., 2024). The critical Ra and drift frequency of wall mode convection with no-slip boundary conditions are presented in Herrmann and Busse (1993); Liao et al. (2006).

Rotating magnetoconvection also exhibits convective multimodality, including oscillatory, wall, magnetic and geostrophic modes (e.g., Sakuraba, 2002; Aujogue et al., 2015; Horn and Aurnou, 2022, 2025). Additionally, a distinct magnetostrophic mode emerges when the dominant force balance occurs between Lorentz and Coriolis forces. This coexistence of these multiple RMC modes occurs within a specific Elsasser number range, which was first identified by Donna Elbert and is referred to here as the Elbert range, following Horn and Aurnou (2022).

The critical Rayleigh numbers and nondimensional frequencies associated with these modes are summarized in Table 1. The frequencies are nondimensionalized by the system’s rotation frequency, $f_\Omega = \Omega/(2\pi)$ with Ω denoting the angular frequency in rad/s. These theoretical values serve as useful references for interpreting the onset behaviors and transitions between convection regimes observed in our experiments.

The oscillatory and wall mode onsets and frequencies for rotating magnetoconvection (RMC) are calculated in Table 1 using the Jupyter Notebook provided in Horn and Aurnou (2022).

Figure 1b shows critical Ra predictions for the different modes of RMC in Earth’s outer core, made using core values of $Ek = 10^{-15}$ and $Pr = 0.1$. The semi-transparent blue shaded box describes the estimated $(Ra-\Lambda)$ param-

ter space ($Ra \in [10^{23}, 10^{29}]$, $\Lambda \in [0.1, 10]$) for RMC in Earth’s outer core (e.g., Gubbins, 2001; Aurnou et al., 2003; Gillet et al., 2010; Roberts and King, 2013; Abbate and Aurnou, 2023). The magnetostrophic, oscillatory and geostrophic convection modes are all strongly supercritical within this region of parameter space; Ra greatly exceeds each mode’s estimated critical values everywhere in the (Λ, Ra) box. This supports the relevance of our multimodal laboratory experimental approach, as it likely mimics the essential dynamics of rotating magnetoconvection in Earth’s outer core, which, based on Figure 1b, is also highly multimodal in nature.

2.3. Transport scalings

Convective velocity scaling predictions can be derived by balancing the kinetic energy production and viscous dissipation terms in the mean kinetic energy equation (e.g., Ingersoll and Pollard, 1982; Aubert et al., 2001; Jones, 2011; King and Buffett, 2013; Hawkins et al., 2023). A generalized expression for the Reynolds number (Re) can be obtained that describes the convective flow:

$$Re \sim \left(\frac{Ra(Nu - 1)}{Pr^2} \right)^{1/2} \frac{\ell}{H}, \quad (9)$$

where ℓ is the characteristic convective flow scale (King and Buffett, 2013) and the Nusselt number, Nu , is the ratio of total and conductive heat transfer (Spiegel, 1971; Goluskin, 2016).

In rotating convective flows, the geostrophic turbulence scale is employed:

$$\ell \sim Ro_c H \sim Ro^{1/2} H, \quad (10)$$

where $Ro = U/(2\Omega H)$ is the Rossby number (Cardin and Olson, 1994; Guervilly et al., 2019; Aurnou et al., 2020). This choice of ℓ leads to the well-known CIA velocity scaling against which we will compare our RC and our RMC data in the following section:

$$Re_{cia} = \left(\frac{Ra(Nu - 1)}{Pr^2} \right)^{2/5} Ek^{1/5}. \quad (11)$$

The CIA scaling is inviscid by construction. However, it may not be free of diffusive effects, a.k.a., fully diffusivity-free (DF), as the heat transport may still depend on the thermal diffusive properties of the fluid. To address this,

we use Julien et al. (2012a)’s diffusivity-free scaling for rotating convective heat transport,

$$Nu - 1 = C_J Ra^{3/2} Ek^2 Pr^{-1/2} = C_J Ro_c^2 Pe_{ff}, \quad (12)$$

where $C_J \approx 1/25$ is a constant derived from their asymptotically-reduced simulations of rapidly rotating convection. Here, $Pe_{ff} = U_{ff}H/\kappa = \sqrt{Ra} Pr$ is the free-fall Péclet number, which estimates the ratio of non-rotating thermal advection and thermal diffusion (Aurnou et al., 2020). The corresponding DF velocity scaling follows by substituting (12) into (11), yielding (Abbate, 2024; Hadjerci et al., 2024; Abbate et al., 2024):

$$Re_{df} = C_J^{2/5} Ro_c^2 Ek^{-1} = C_J^{2/5} Ro_c Re_{ff}, \quad (13)$$

where $C_J^{2/5} \approx 0.276$.

A separate heuristic velocity scaling was postulated in King and Buffett (2013) to describe magnetostrophic convection. However, we have been unable to collapse any of our velocity data with this Re_{mac} scaling, and, thus, will not consider it further in this study.

3. Methods

3.1. Laboratory set-up and diagnostics

Figure 2a shows a photograph of the experimental set-up, ‘RoMag’. The test section consists of top and bottom copper lids and a cylindrical stainless steel sidewall section situated between the lids. The bottom lid is heated by a basal heat pad, which provides an input heating power of $P = 0$ to 780 W. The applied heating is removed from the top lid by a heat exchanger connected to a recirculating thermostated chiller. This equipment is mounted on a rotating pedestal. The test section is insulated with a 1 cm thick layer of aerogel, which has a thermal conductivity of approximately $k = 0.015$ W/(m K). The working fluid is gallium, which has a Prandtl number $Pr \approx 0.026$. Gallium’s thermal conductivity is $k = 31.4$ W/(m k) and the kinematic viscosity of the gallium is $\nu = 3.4 \times 10^{-7}$ m² / s (Aurnou et al., 2018). For further RoMag device details, see King et al. (2012).

Figure 2b contains a schematic of the test section. The dimensions of the fluid volume are $H = 9.84$ cm in height and $R = 9.84$ cm in radius, yielding $\Gamma = 2R/H = 2$. A nearly uniform vertical magnetic field is applied by an

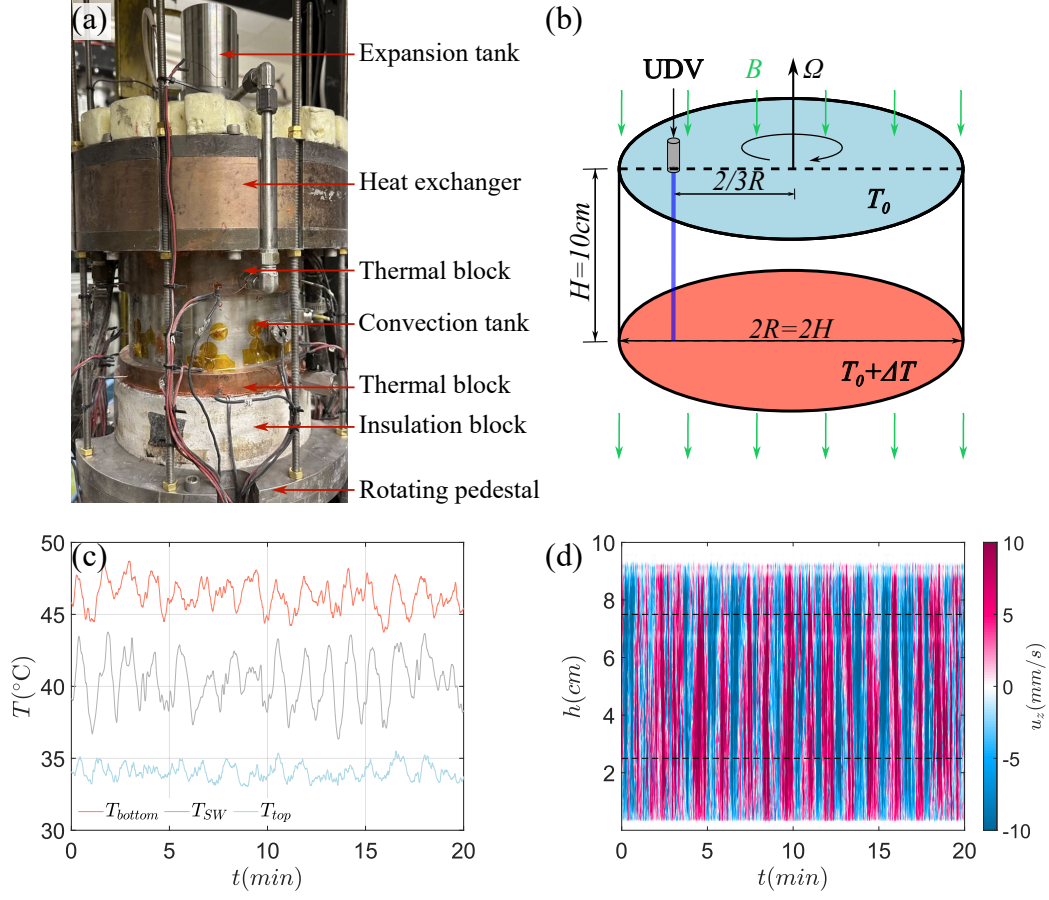


Figure 2: (a) A photograph of the RoMag set-up with aspect ratio $\Gamma = 2R/H = 2$ tank ($H = 9.84$ cm; $R = 9.84$ cm) used here. (b) schematic of the convection cell showing the ultrasonic Doppler velocimetry (UDV) measurements and the imposed temperature, rotation and magnetic fields; (c,d) examples of temperature and velocity signals obtained from an RC case carried out at $Ra = 3.08 \times 10^6$ ($P = 780$ W) and $Ek = 10^{-4}$ (1.78 rpm).

external solenoid, generating a magnetic flux density of up to 0.2 T. The tank is spun here between 0 and 36 revolutions per minute (rpm) in a left-handed sense. Due to this left-handed applied rotation, a left-handed (s, ϕ, z) coordinate system is used here, with $z = 0$ cm defining the base of the fluid layer. The top and bottom lids each contain six embedded thermistors used to measure the bottom to top temperature difference $\Delta T = (T_{bottom} - T_{top})$ across the fluid layer. With this information, the Nusselt number can be

computed as:

$$Nu = qH/(k\Delta T), \quad (14)$$

where $q = P/(\pi R^2)$ is the heat flux from the basal heat pad, corrected for any sidewall losses. The midplane ($z = H/2$) temperature is monitored by 12 equally spaced thermistors situated on the exterior face of the sidewall. Examples of the individual thermistor signals obtained from the bottom lid (T_{bottom}), the side-wall (T_{SW}) and the top lid (T_{top}) are shown in Figure 2c.

Convective flow velocities in the liquid metal are experimentally measured using the non-invasive ultrasonic Doppler velocimetry (UDV) technique (Takeda, 1995; Brito et al., 2001). Yielding a chord of velocity data along the UDV transducer's line of sight (Figure 2b), UDV has been successfully applied to obtain velocity profiles in fluids that are both transparent (e.g., Noir et al., 2001; Brito et al., 2004) and opaque (e.g., Aubert et al., 2001; Vogt et al., 2018; Zürner et al., 2019; Vogt et al., 2021a; Cheng et al., 2022). In this study, we employ the DOP5000 UDV system (Signal Processing SA, Switzerland), operating at an emission frequency of $f_e = 8$ MHz, and equipped with a vertically-oriented piezoelectric ceramic transducer. This UDV probe is positioned in the top lid at $2R/3$ from the container's center to measure the instantaneous vertical velocity component u_z across the entire fluid layer height. A Hovmöller diagram of UDV u_z data is plotted in Figure 2d.

The root mean square (RMS) value of the vertical UDV velocity, $u_{z,rms}$, is evaluated over time and over the height range from $0.25H$ to $0.75H$ (see the two horizontal dashed lines in Figure 2d):

$$u_{z,rms} = \sqrt{\frac{1}{N_t N_z} \sum_{i=1}^{N_t} \sum_{j=1}^{N_z} u_z^2(z_j, t_i)}. \quad (15)$$

This then allows us to calculate the experimentally measured axial Reynolds number as:

$$Re_z = \frac{u_{z,rms} H}{\nu}. \quad (16)$$

Following that, the experimentally measured Rossby number is calculated via:

$$Ro_z = \frac{u_{z,rms}}{2\Omega H} = \frac{u_{z,rms} H}{\nu} \frac{\nu}{2\Omega H^2} = Re_z Ek. \quad (17)$$

We estimate the peak axial velocity, $u_{z,max}$, by identifying the maximum

value of the height-averaged velocity:

$$u_{z,\max} = \max \left(\frac{1}{N_z} \sum_{j=1}^{N_z} u_z(z_j, t_i) \right), \quad (18)$$

which we will use in (7) to calculate N_ℓ . Since the axial velocities do not greatly vary in value in z this scheme acts mainly to filter out any spurious high velocity values while retaining physically-meaningful peak velocity signatures.

3.2. Parameter space

Figure 3a plots the experimental parameter space investigated. Hollow circles correspond to $\Lambda = 0$ RC cases, whereas solid circles denote $\Lambda = 1$ RMC cases. Symbol color denotes the experimental rotation rates, corresponding to Ekman numbers of $Ek = 10^{-4}$, 4×10^{-5} , 2×10^{-5} and 10^{-5} . The RC cases have all been slightly displaced to the left so that they are not hidden in the plot by the solid RMC symbols.

At each Ek value, the input power P was systematically changed in order to vary the buoyancy forcing (Ra). The convective supercriticality of each case, \widetilde{Ra}_{min} , is shown on the y-axis. Here we define supercriticality as

$$\widetilde{Ra}_{min} = Ra / Ra_{crit,min}$$

where

$$Ra_{crit,min} = \min\{Ra_o^\infty, Ra_o^{cyl}, Ra_w^\infty, Ra_s^\infty, Ra_{mac}^\infty\}.$$

In the RC cases, Ra_{mac}^∞ is not considered in calculating \widetilde{Ra}_{min} .

Figures 3b and 3c show the different modes critical Ra curves as a function of the Elsasser number Λ for liquid Gallium ($Pr = 0.025$) at $Ek = 10^{-4}$ and $Ek = 10^{-5}$, respectively, all computed via Horn and Aurnou (2022)'s Jupyter notebook. Additionally, the cyan triangles mark Ra_o^{cyl} in a $\Gamma = 2$ cylindrical tank (Zhang and Liao, 2009). In both these panels, with increasing Ra , RC first develops via the bulk oscillatory mode (cyan dotted line / cyan triangle), followed by the development of the wall mode (green dashed line), and finally the stationary geostrophic mode (gold solid line). In contrast, $\Lambda = 1$ RMC has a different sequence of modal development. RMC initially manifests as a wall mode, followed nearly immediately by the emergence of the oscillatory mode, then the stationary magnetostrophic mode (pink solid line), and finally the stationary geostrophic mode.

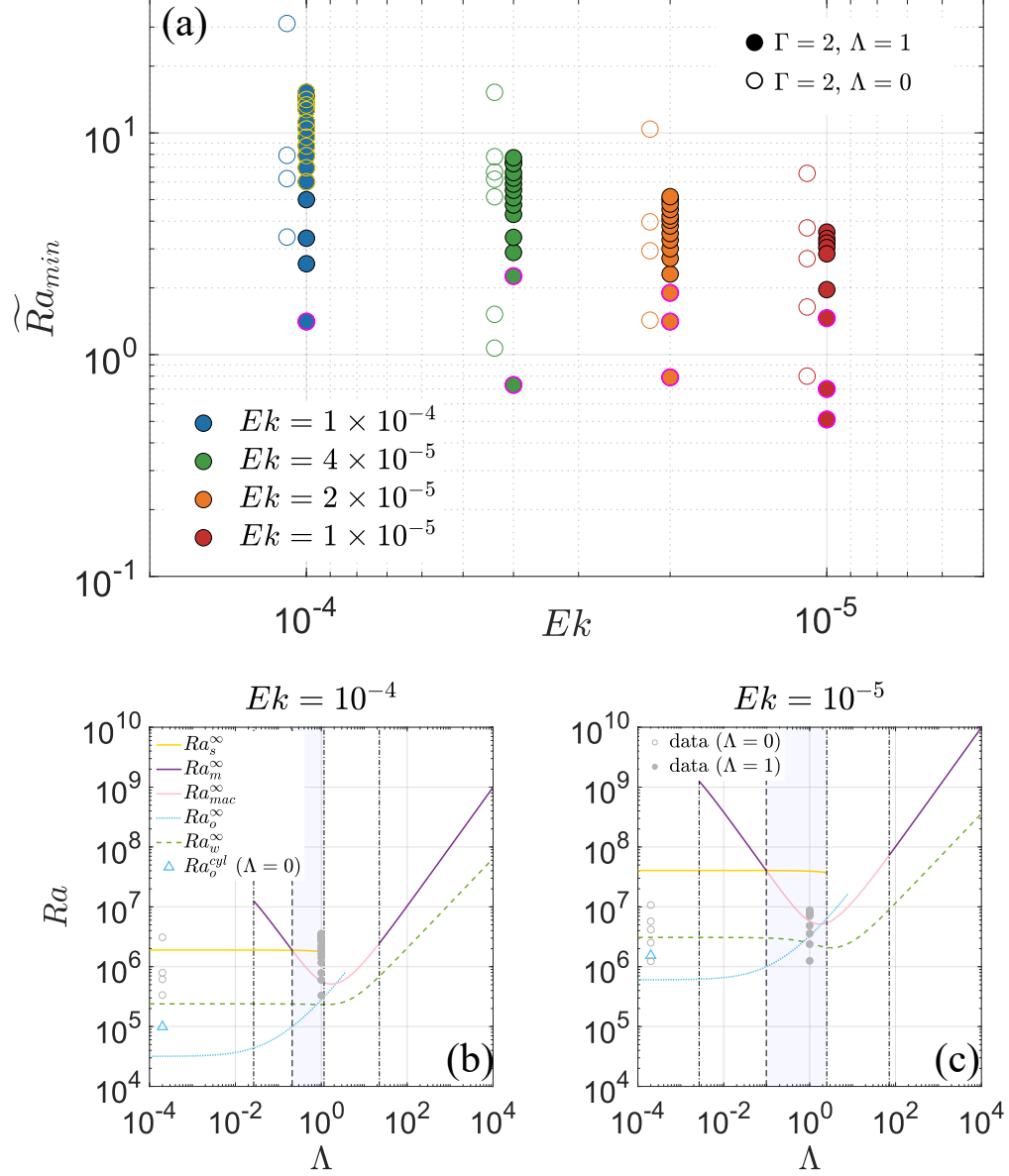


Figure 3: (a) Experimental $(Ek, Ra/Ra_{crit,min})$ parameter space, where Ra_{min} is the minimum of all the critical Ra values. Hollow RC symbols are offset in Ek for visibility. Gold edge color indicates cases in geostrophic regime, magenta edge color marks cases where the magnetostrophic mode is not active. Liquid gallium critical Ra predictions from Horn and Aurnou (2022) for (b) $Ek = 10^{-4}$ and (c) $Ek = 10^{-5}$. Hollow (filled) circles denote RC (RMC) experiments.

Input and output parameter values for all the experimental cases are provided in the data tables in the Appendix.

3.3. Validation cases

Figure 4 presents sidewall thermal measurements for two $Ek = 4 \times 10^{-5}$ RC cases conducted to assess the accuracy and reliability of our experimental configuration under different convective regimes. In the first case, $Ra = 4.4 \times 10^5$, which just exceeds the onset value for the oscillatory mode in a cylindrical geometry ($Ra/Ra_o^\infty = 4.4$, $Ra/Ra_w = 0.64$). In the second case,

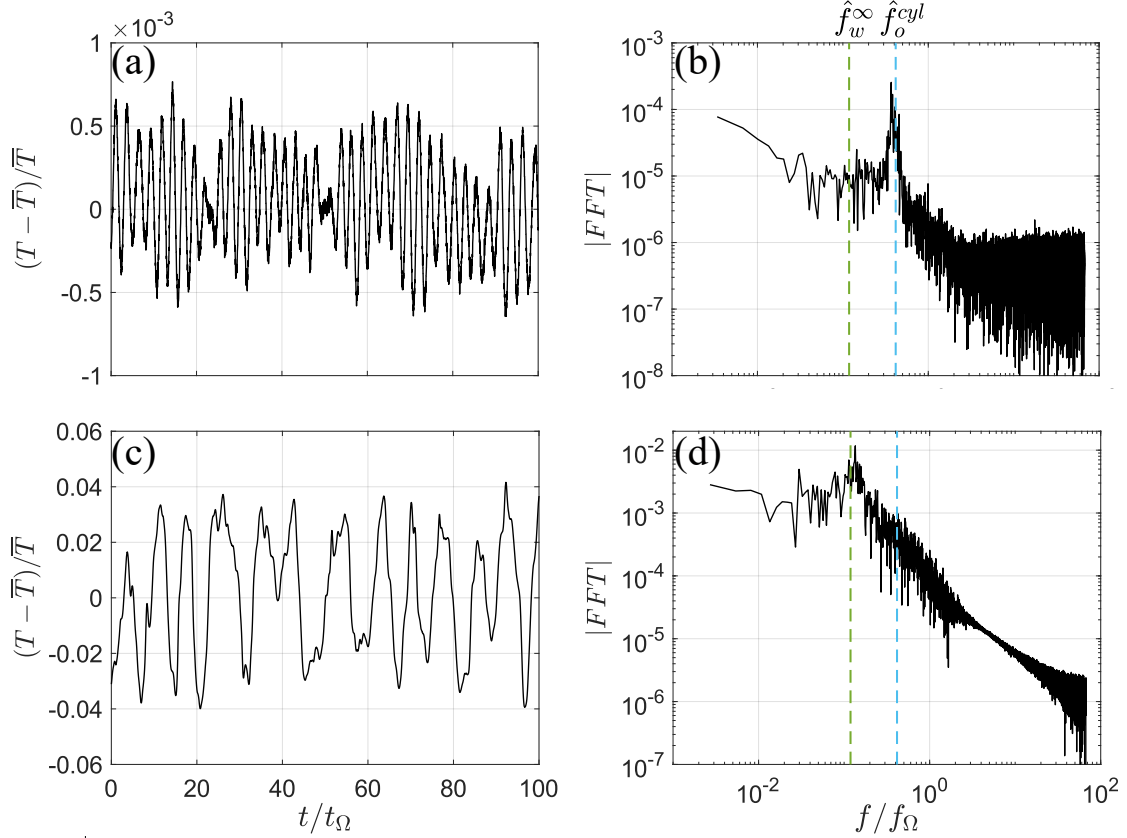


Figure 4: Validation cases for side-wall thermistor measurements of oscillatory and wall modes at $Ek = 4 \times 10^{-5}$ and $\Lambda = 0$: (a,c) normalized side wall temperature (located at 270°) fluctuations at $Ra = 4.41 \times 10^5$ ($Ra/Ra_o^\infty = 4.4$, $Ra/Ra_w = 0.64$) and $Ra = 1.93 \times 10^6$ ($Ra/Ra_o^\infty = 19.3$, $Ra/Ra_w = 2.8$); (b,d) corresponding amplitude of the Fourier Transform of temperature fluctuations in (a,c).

$Ra = 1.9 \times 10^6$ such that its wall modes are active as well ($Ra/Ra_o^\infty = 19.3$, $Ra/Ra_w = 2.8$).

Figures 4a and 4c show the time series of normalized temperature fluctuations, $(T - \bar{T})/\bar{T}$, measured by the mid-height side-wall thermistor positioned at 270° , where \bar{T} is the mean value of the time series. The time axes are nondimensionalized by the system's rotation period $t_\Omega = 2\pi/\Omega$. Both signals exhibit periodic oscillations. However, the bulk oscillations in (a) are higher frequency and have a very low amplitude when measured on the exterior sidewall. In contrast, the wall modes are lower frequency and are far larger in amplitude when measured on by these exterior sidewall situated sensors.

Corresponding Fourier spectra are shown in Figures 4b and 4d with the frequency axis nondimensionalized using the system's rotation frequency $f_\Omega = t_\Omega^{-1} = \Omega/(2\pi)$. In (b), a strong spectral peak aligns with the predicted oscillation frequency for cylindrical geometry, $\hat{f}_o^{cyl} = f_o^{cyl}/f_\Omega$ (vertical cyan dashed line). In (d), the wall mode generates the dominant spectral peak near the predicted wall mode frequency for a semi-infinite plane layer, $\hat{f}_w^\infty = f_w^\infty/f_\Omega$ (vertical green dashed line). These cases successfully validate that our laboratory set-up generates convective flows that are in good agreement with the predictions for low Pr RC, and, further, that the characteristics of different convective modes are detectable and distinguishable.

4. Results

4.1. Flow fields

Figure 5 shows the spatiotemporal evolution of vertical velocity u_z measured using the vertical UDV for four different cases. The left column corresponds to rotating convection (RC) at Ekman numbers $Ek = 10^{-4}$ and $Ek = 10^{-5}$, while the right column represents RMC under the same Ekman numbers but with $\Lambda = 1$. The vertical axis denotes the spatial coordinate along the tank height (H), while the horizontal axis represents the dimensionless rotational time (t/t_Ω). The details of the supercriticality and parameter values for these cases are provided in Table 2.

A comparison of Figures 5a and 5b reveal that both cases exhibit flow oscillations of comparable amplitude, spanning the system scale (H). However, the presence of the magnetic field in the RMC yields a lower oscillation frequency. Both cases are unstable to the geostrophic mode, with supercriticality $\widetilde{Ra}_s^\infty = 1.6$ and 2.0, respectively, as predicted by linear theory for an

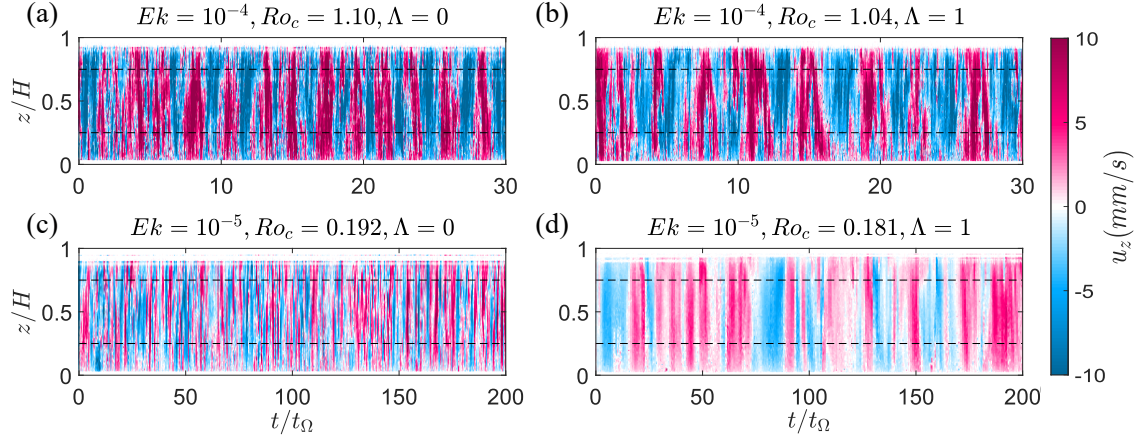


Figure 5: Hovmöller diagrams of vertical velocities obtained from the vertical UDV probe. Left column $\Lambda = 0$ and right column $\Lambda = 1$; top row $Ek = 10^{-4}$ and bottom row $Ek = 10^{-5}$; input power $P = 780W$ for all cases; Rayleigh numbers: (a) $Ra = 3.08 \times 10^6$; (b) $Ra = 3.57 \times 10^6$; (c) $Ra = 1.01 \times 10^7$; (d) $Ra = 8.80 \times 10^6$.

Fig. 5	Λ	$Ek \cdot 10^4$	$Ra \cdot 10^{-6}$	Ro_c	\widetilde{Ra}_o^∞	\widetilde{Ra}_o^{cyl}	\widetilde{Ra}_w^∞	$\widetilde{Ra}_{mac}^\infty$	\widetilde{Ra}_s^∞	Nu	Re_z	Ro_z
(a)	0	1	3.08	1.04	97.0	31.2	12.9	—	1.6	6.69	2565	0.2565
(b)	1	1	3.57	1.10	12.7	—	15.3	6.2	2.0	5.96	2005	0.2005
(c)	0	0.1	10.10	0.192	16.7	6.6	3.3	—	0.2	2.14	1289	0.0129
(d)	1	0.1	8.60	0.181	2.7	—	3.6	1.5	0.2	2.47	691	0.0069

Table 2: Input and output parameters for the cases shown in Figure 5. The definitions of these parameters are provided in Sections 2.1, 3.1 and 3.2.

infinite plane layer. However, the flow remains predominantly governed by the oscillatory mode. This discrepancy may arise from an underestimation inherent in the linear theoretical planar prediction, relative to that of an actual cylinder. Although the convective Rossby number for both $Ek = 10^{-4}$ cases is approximately unity (~ 1), their spectra each show a peak consistent with oscillatory behavior. The $\Lambda = 0$ case exhibits a strong peak near the predicted oscillatory RC frequency, while the $\Lambda = 1$ case also shows an oscillatory peak, albeit weaker and shifted to a lower frequency, consistent with a slowed RMC oscillation prediction (see Figure A.12 in the Appendix).

Figure panels 5c and 5d allow us to compare the RC and RMC Hovmöller UDV diagrams at a lower Ekman number, $Ek = 10^{-5}$, over a 200 rotation period time window. Comparing the two cases, it is evident that the imposition of a vertical magnetic field, such that $\Lambda = 1$, lowers the intensity of

the RMC flow and causes it to become better aligned in the axial direction. Thus, a larger-scale flow structure emerges in the RMC case, consistent with findings from numerical simulations of Rayleigh-Bénard convection with a vertically imposed magnetic field (e.g., Yan et al., 2019). There is no fundamental change in the gross flow structures in all four Hovmöllers: the axial velocities generally remain locally well aligned with the axis of the rotating tank $\hat{\mathbf{z}}$. These results are quantitatively consistent with, and compare well to, the laboratory-numerical liquid metal RC experiments of Vogt et al. (2021a). It is interesting that this axiality appears to remain intact, although the convective Rossby numbers are near unity in the higher Ek cases, while being closer to 0.2 in the lower Ek cases. However, for the low Ro_c $\Lambda = 1$ case, it is clear that slower, larger-scale, coherent motions dominate the system, in qualitative agreement with magnetostrophic theory and with simulation results such as those of Yadav et al. (2016b).

4.2. Heat and momentum transport

4.2.1. Scaling with supercriticality

Figure 6a shows the convective heat transfer, $Nu - 1$, as a function of supercriticality, $\widetilde{Ra} = Ra/Ra_o^{cyl}$, for rotating convection (hollow circles) and rotating magnetoconvection (filled circles). All the heat transfer data is moderately well collapsed as a function of \widetilde{Ra}_o^{cyl} . For $Ek < 10^{-4}$, the RMC $\Lambda = 1$ heat transfer is enhanced relative to the RC cases, and this enhancement becomes more pronounced as the Ekman number Ek decreases. These observations are consistent with previous experimental (King and Aurnou, 2015; Grannan et al., 2022) and numerical (Yadav et al., 2016a) results. It was argued in Grannan et al. (2022) that this enhancement was due to the presence of magnetostrophic wall modes (Grannan et al., 2022). Based on Figure 5d, it appears plausible that the $\Lambda = 1$ heat transfer enhancement here is due to large-scale, slightly lower velocity, coherent bulk flows (cf. Chong et al., 2017; Xia et al., 2023).

Figure 6b presents the vertical Reynolds number Re_z normalized by the CIA-predicted Reynolds number Re_{cia} , where the characteristic flow scale is taken to be the experimentally-measurable $\ell \sim Ro^{1/2}H$ (Cardin and Olson, 1994; Guervilly et al., 2019). For $\widetilde{Ra}_o^{cyl} \gtrsim 8$, the RC and RMC data collapse well and tend toward Re_{cia} (solid black horizontal line). In contrast, we find for $\widetilde{Ra}_o^{cyl} < 8$ that the RC data remain close to Re_{cia} , whilst the RMC data fall significantly below Re_{cia} . We argue that this is due to magnetic damping.

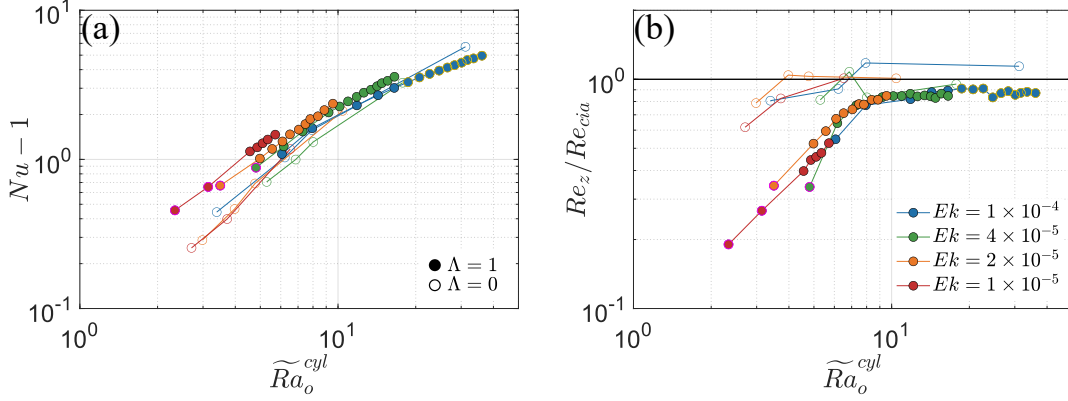


Figure 6: (a) Convective heat flux relative to conduction heat flux $Nu - 1$ and (b) vertical Reynolds number normalized by the CIA scaling prediction, Re_z/Re_{cia} , as a function of the cylindrical supercriticality, \widetilde{Ra}_o^{cyl} for rotating convection data (hollow circle) and rotating magnetoconvection data (filled circle). Gold edge color indicates cases in geostrophic regime, magenta edge color marks cases where the magnetostrophic mode is not active.

Overall, the thermovelocimetric data in Figures 5 and 6 support the fundamental predictions for magnetostrophic convection: coherent, larger-scale, magnetically-damped flows act to enhance the global heat transfer.

As the magnetostrophic mode is essentially inertia-less, inertial forces are expected to be small compared to the Coriolis and Lorentz forces (Roberts and King, 2013; Horn and Aurnou, 2022). To quantify the relative importance of inertia, we turn to the local interaction parameter N_ℓ and the convective interaction parameter N_c , respectively defined in equations (7) and (8). To compute N_ℓ , we use the maximum vertical velocity $u_{z,max}$ defined in equation (18). This choice of velocity is better suited for capturing the dynamics of oscillatory flows.

Figure 7 shows Re_z/Re_{cia} plotted as a function of supercriticality \widetilde{Ra}_o^{cyl} , similar to Figure 6b. However, here the symbol fill color represents either (a) N_ℓ or (b) N_c , and the edge color indicates the Ekman number Ek . We observe that both N_ℓ and N_c approach values near 3 at the knick point near $\widetilde{Ra}_o^{cyl} \approx 8$. To estimate the critical N values, we perform separate power-law fits to the data for $\widetilde{Ra}_o^{cyl} < 8$ and $\widetilde{Ra}_o^{cyl} \geq 8$ (shown as blue and red dashed lines in Figure 7). The averaged values near the intersection point of the two fits give transitions values of $N_\ell \approx 4.0$ and $N_c \approx 3.1$, indicating that both

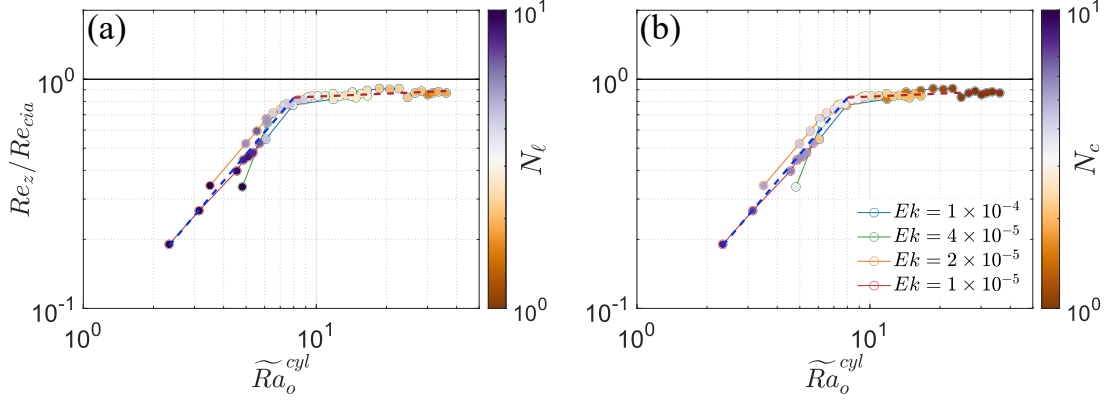


Figure 7: Vertical Reynolds number normalized by the CIA scaling prediction, Re_z/Re_{cia} , plotted as a function of the cylindrical superficiality parameter, \widetilde{Ra}_o^{cyl} . The data are the same rotating magnetoconvection (RMC) measurements shown in Figure 6, with marker edge colors indicating the Ekman number Ek , and marker fill colors representing: (a) the local interaction parameter N_ℓ , and (b) the convective interaction parameter N_c . The blue dashed line shows a power-law fit to data with $\widetilde{Ra}_o^{cyl} < 8$, while the dark red dashed line corresponds to a fit over the range $\widetilde{Ra}_o^{cyl} \geq 8$. The intersection of the two fits give the transition values of $N_\ell \approx 4.0$ and $N_c \approx 3.1$.

parameters are on the order of unity. The critical values of the interaction parameters indicate a transition from a magnetostrophic regime above the transition value to geostrophic turbulence below the transition value. Both the local interaction parameter N_ℓ and the convective interaction parameter N_c exhibit a similar critical threshold value of around 3 to 4. While N_ℓ is defined based on the measured convective velocity (an output quantity), N_c is formulated using the input control parameters.

Figure 8 presents N_ℓ as a function of N_c , enabling direct comparison between these two interaction parameter definitions. The figure reveals that N_ℓ closely follows N_c across most RMC cases, with the exception of data points that are near the onset point of magnetostrophic convection, which are highlighted with magenta edge colors in Figure 8. To quantify their relationship, we performed a power-law fit to the data with $N_\ell \geq 3$, yielding the empirical relation $N_\ell = (1.11 \pm 0.15) N_c^{1.14 \pm 0.14}$. This strong, approximately linear correspondence between N_ℓ and N_c across most cases suggests that the convective interaction parameter, which is based solely on input parameters, can serve as a reliable proxy for characterizing the flow regime relatively near

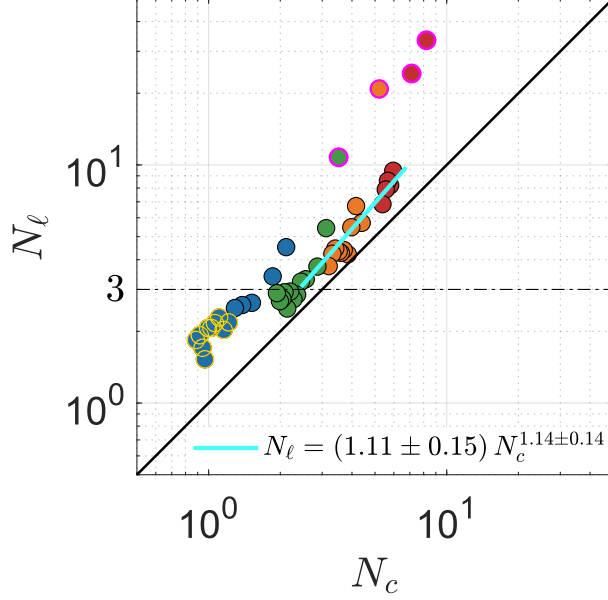


Figure 8: Local interaction parameter N_ℓ versus convective interaction parameter N_c for RMC data, gold edge color indicates cases in geostrophic regime, magenta edge color marks cases where the magnetostrophic mode is not active, cyan dashed line is the best of the data with $N_\ell \geq 3$ and magnetostrophic unstable (magenta edge color data excluded), black solid line represents $N_\ell = N_c$, black dot-dashed line indicates $N_\ell = 3$.

$N_\ell \approx N_c \gtrsim 3$. However, since N_ℓ can be directly obtained from our measurements and makes no assumptions on flow velocities or scales, we will use it to predict the Reynolds number under Earth's core conditions in Section 5.

4.2.2. Diffusivity-free scaling

In rotating convection, the ultimate regime—also referred to as the diffusivity-free (DF) regime—describes the limit in which inertia, buoyancy, and Coriolis forces dominate the flow dynamics, while viscous and thermal diffusivities become negligible (Julien et al., 2012a; Aurnou et al., 2020). The DF regime likely best describes rotating convective turbulence in $\Lambda \ll 1$ planetary and stellar fluid systems (Aurnou et al., 2015). Evidence supporting this DF scaling has emerged in recent studies (Lepot et al., 2018; Hadjerci et al., 2024; Abbate, 2024; Abbate et al., 2024). For instance, Abbate (2024) and Abbate et al. (2024) demonstrate that the heat transfer, internal tem-

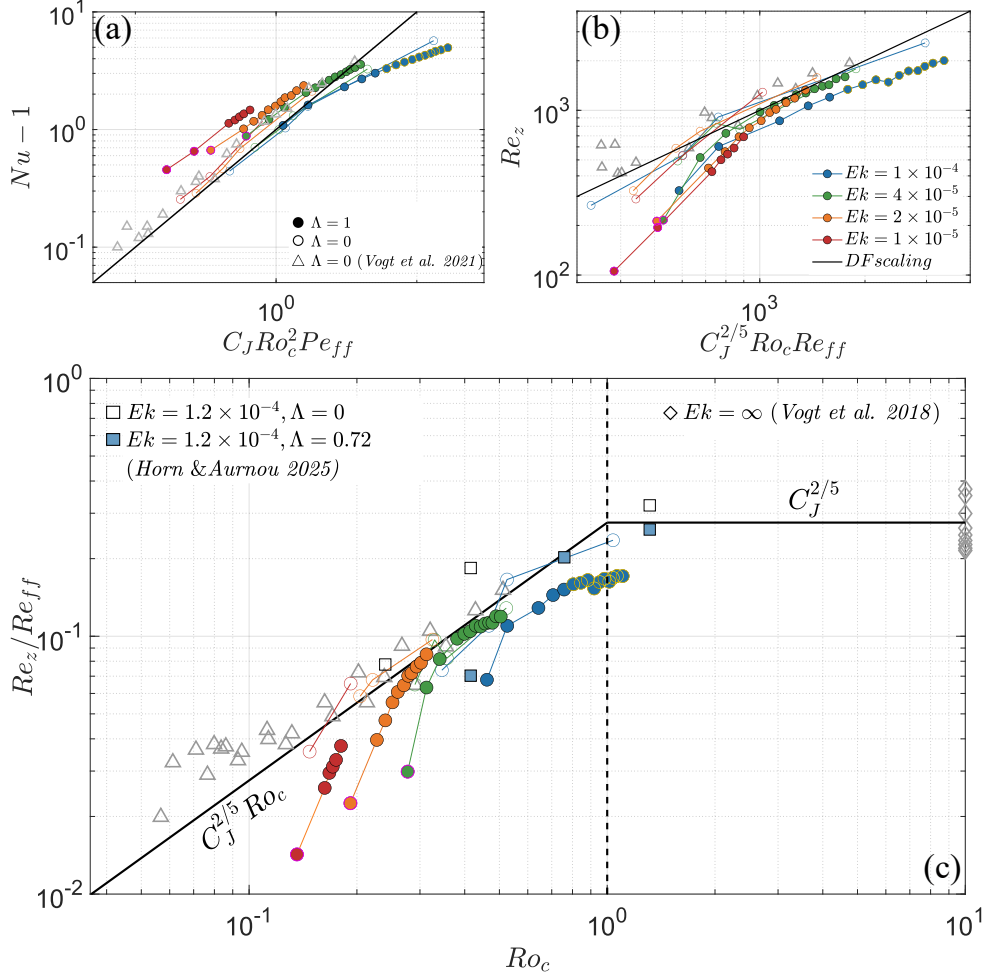


Figure 9: (a) Convective heat flux relative to conduction heat flux $Nu - 1$ as a function of the diffusivity free prediction $C_J Ro_c^2 Pe_{ff}$; (b) vertical Reynolds number Re_z as a function of diffusivity free prediction $C_J^{2/5} Ro_c Re_{ff}$; (c) vertical Reynolds number Re_z , normalized by the free-fall Reynolds number Re_{ff} , plotted as a function of the convective Rossby number Ro_c . The diagonal black solid line shows the diffusivity-free prediction for $Ro_c \ll 1$ and the horizontal black solid line is the diffusivity-free prediction for $Ro_c \gg 1$ (Aurnou et al., 2020). Filled circles with pink edges indicate cases with $Ra < \widetilde{Ra}_s^\infty$; filled circles with gold edges indicate cases with $Ra > \widetilde{Ra}_s^\infty$. The grey diamonds denote RBC ($Ek = \infty$, $Ch = 0$) data from Vogt et al. (2018); the grey triangles mark rotating convection data from Vogt et al. (2021a); hollow squares ($\Lambda = 0$) and blue filled squares ($\Lambda = 0.72$) denote DNS data from Horn and Aurnou (2025) at $Ek = 1.2 \times 10^{-4}$ with aspect ratio $\Gamma = 8$.

perature fluctuations, and flow velocities associated with the thermal-inertial oscillatory mode in liquid metal convection are consistent with DF scaling predictions.

We test our RMC data against the DF scaling to determine whether the flow is dominated by inertial or Lorentz forces. The convective heat transfer, $Nu - 1$, is plotted as a function of the DF scaling parameter $C_J Ro_c^2 Pe_{ff}$ in Figure 9a, where the pre-factor $C_J = 1/25$ is taken from Julien et al. (2012a). Both RC and RMC data generally follow the DF scaling (solid black line), with only the data at $Ek = 10^{-4}$ deviating below this trend (Abbate et al., 2024). The RMC data at $Ek = 10^{-5}$ exhibit a similar slope to the DF scaling but are shifted upward, which is due to the higher heat transfer efficiency found in these magnetostrophic convection cases.

Figure 9b plots the vertical Reynolds number Re_z as a function of the DF scaling prediction $C_J^{2/5} Ro_c Re_{ff}$ for RC and RMC cases. The velocity data for RC (hollow circles and triangles) align well with the DF scaling. In contrast, the RMC data (filled circles) exhibit a transition around $Re_z \approx 800$. Below this threshold, the velocities are suppressed by the magnetic field and fall below the DF scaling prediction. Above this threshold, the inertial effect is still dominant and the RMC data also follow the DF scaling. Notably, the suppression of convective velocity corresponds with enhanced convective heat transfer, arising from increased coherence of the convective flow (see Figure 5c,d), a mechanism also observed in turbulent Rayleigh–Bénard convection (Huang et al., 2013; Chen et al., 2023).

Figure 9c shows the vertical Reynolds number normalized by the free-fall Reynolds number Re_z/Re_{ff} plotted against the convective Rossby number Ro_c . Following Abbate et al. (2024), the inclined and horizontal black solid lines, respectively, represent the DF scaling $C_J^{2/5} Ro_c$ for rotating convection (RC) and $C_J^{2/5}$ for Rayleigh–Bénard convection (RBC). The RC data, shown as hollow circles and triangles, follow the DF scaling. In contrast, the RMC data fall below the DF scaling but gradually approach it as Ro_c increases.

Unfortunately, no low Pr , slowly rotating ($Ro_c > 1$) RC data exists to plot on the right side on Figure 9c. In place of this missing data, the non-rotating, non-magnetic liquid gallium RBC data from Vogt et al. (2018) are included in this plot as hollow grey diamonds. The $Ek = \infty$ data, plotted on the right edge of the figure, are well aligned with the non-rotating diffusivity-free scaling prediction using the Julien et al. (2012a) prefactor $C_J^{2/5} \approx 0.276$.

Figure 9c also includes Horn and Aurnou (2025)’s $\Gamma = 8$ cylindrical direct

numerical simulation (DNS) data at $Ek = 1.2 \times 10^{-4}$ (hollow square (RC $\Lambda = 0$ data); blue-filled square (RMC $\Lambda = 0.72$ data)). Their $\Lambda = 0.72$ RMC simulations exhibit lower Reynolds numbers compared to RC cases, consistent with our experimental observations. Their DNS data with $Ro_c > 1$ align with the predicted slowly rotating DF scaling.

Overall, the rapidly rotating ($Ro_c < 1$) RC data in Figure 9c align well with the rapidly rotating DF predictions, $Re \simeq C_J^{2/5} Ro_c Re_{ff}$ (Abbate et al., 2024). Further, in the slowly (or non-rotating) $Ro_c \gg 1$ regime, we find that $Re \simeq C_J^{2/5} Re_{ff}$. The data in the slowly rotating regime ($Ro_c \gtrsim 1$) at high- Pr fluids are available in Abbate and Aurnou (2023, 2024), whereas data for low- Pr fluids are currently lacking, and future experiments are needed to confirm the asymptotic slowly rotating scaling. Since all the RMC data lie below the RC data, this implies that the asymptotic, DF RC scalings provide good first-order bounding estimates for convective velocities in planetary-core and subsurface ocean environments.

5. Planetary applications

To further investigate the $N_\ell \approx 3$ transition between geostrophic and magnetically-damped convection, Figure 10 plots the $\Lambda = 1$ Re_z data normalized by the diffusivity-free RC scaling prediction, Re/Re_{df} as a function of N_ℓ . While the Reynolds number is denoted as Re_z in prior experiments to indicate its vertical component, we generalize the notation to Re in this section. We use Re_{df} as the normalization here (instead of Re_{cia} as used in Figure 7) because Re_{df} better extrapolates to planetary settings, where diffusivity-free turbulence is argued to dominate bulk convective flows (Stevenson, 1979; Julien et al., 2012b; Barker et al., 2014; Bouillaut et al., 2021; Abbate et al., 2024; van Kan et al., 2025).

The magnetically-damped, $N_\ell \geq 3$ data collapse moderately well in Figure 10. We therefore perform a fit to the $N_\ell \geq 3$ data, excluding one outlier from the $Ek = 1 \times 10^{-4}$ dataset and the magenta-edged points in which the magnetostrophic convective mode is not active. We refer to the resulting scaling as the magnetically damped Reynolds number, Re_{MD} , which is fit as follows:

$$Re_{MD} = c Re_{df} N_\ell^\alpha, \quad (19)$$

The best fit to (19) is shown as the black dotted line in Figure 10, with corresponding best fit parameter values of $c = 1.72 \pm 0.14 \approx 2$ and $\alpha =$

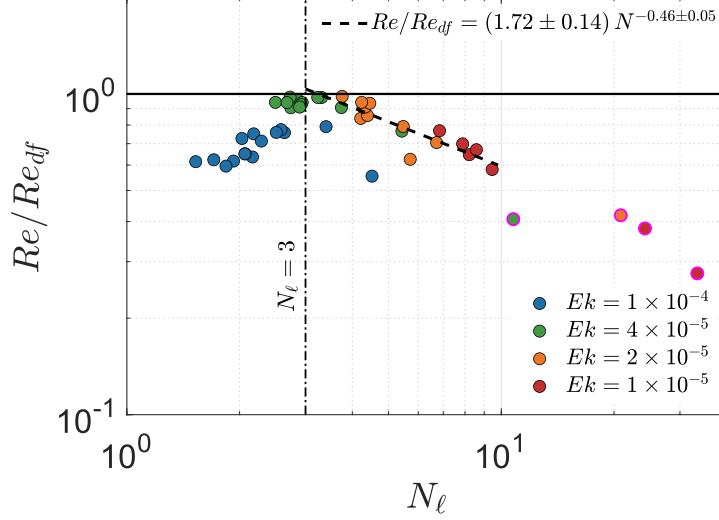


Figure 10: Reynolds number normalized by the diffusion-free RC scaling prediction, Re/Re_{df} , plotted as a function of local interaction parameter N_ℓ for RMC data, black dashed line is the best fit the data with $N_\ell \leq 3$ (data at $Ek = 1 \times 10^{-4}$ and magnetostrophic stable data (pink edge color) are not included), vertical black dot-dashed line is $N_\ell = 3$, and horizontal black solid line represents $Re_z = Re_{df}$.

$-0.46 \pm 0.05 \approx -1/2$. The data that do not have active magnetostrophic modes (magenta edge color) are not included in the above fit. However, even when these points are included, the best fit exponent remains near $-1/2$, with $\alpha = -0.53 \pm 0.03$.

Thus, the empirical best fit for Re_{MD}/Re_{df} is

$$\frac{Re_{MD}}{Re_{df}} \approx \frac{2}{N_\ell^{1/2}}, \quad \text{for } N_\ell \gtrsim 3, \quad (20)$$

noting that this relationship holds only in the quasi-static, low local magnetic Reynolds number limit that applies to our laboratory liquid metal MHD experiments. This $Re \sim N_\ell^{-1/2} \propto |B|^{-1}$ relation shows that the convective flow velocities are reduced with increasing Lorentz forces (i.e., higher N_ℓ) from the axially imposed magnetic field (cf. Vogt et al., 2021b).

We recast (20) into a piecewise, regime-dependent form to provide a unified prediction of the Reynolds number across both weakly and strongly

magnetically influenced regimes:

$$Re \approx \begin{cases} Re_{df} & \text{for } N_\ell \lesssim 3 \\ 2N_\ell^{-1/2} Re_{df} & \text{for } N_\ell \gtrsim 3 \end{cases} \quad (21)$$

This form offers a practical framework for estimating planetary core convective velocities based on the local interaction parameter, and highlights the critical threshold $N_\ell \approx 3$ where magnetic damping becomes pronounced.

Alternatively, it is possible to formulate an equivalent scaling expression for Re_{MD} in terms of input parameters. This is accomplished by substituting (7) into (19), and then by approximating the characteristic length scale to be $\ell = Ro_c H$, which holds in and near the geostrophic turbulence regime (Yadav et al., 2016b; Aurnou and King, 2017). By doing so, we obtain:

$$\begin{aligned} Re_{MD} &= c Re_{df} \left(\frac{\sigma B^2 \ell}{\rho U} \right)^\alpha \\ &= c Re_{df} \left(\frac{\sigma B^2 (Ro_c H)}{\rho U} \right)^\alpha \\ &= c (C_J^{2/5} Ro_c Re_{ff}) \left(\frac{Ch Ro_c}{Re_{MD}} \right)^\alpha \end{aligned} \quad (22)$$

Recasting (22) using our best-fit empirical values, $c \approx 2$ and $\alpha \approx -1/2$, then yields:

$$Re_{MD} = 4C_J^{4/5} \left(\frac{Ra Ek}{Pr} \right)^{3/2} \frac{Ek^{1/2}}{\Lambda} = 4C_J^{4/5} Ro_c^3 (Ek \Lambda)^{-1}, \quad (23)$$

where $4C_J^{4/5} \approx 0.3$. Expression (23) captures the $N_\ell \gtrsim 3$ dependence of the magnetically damped Reynolds number solely using input parameters. This enables us to make predictions of convective flow velocities in the magnetostrophic $\Lambda \sim 1$ regime without requiring direct velocity measurements.

The convective interaction parameter N_c and the local interaction parameter N_ℓ are nearly equivalent in our $N_\ell \gtrsim 3$ data (Figure 8). Either of these parameters can therefore be used to predict the corresponding interaction parameter range in Earth's outer core. However, N_c is computed directly from the input parameters (Ra , Ek , Pr , and Λ), whereas N_ℓ requires estimates of the flow scales and velocity, which are difficult to accurately obtain. We therefore use N_c to estimate the convective interaction parameter range relevant to Earth's core.

Figure 11a shows predictions of N_c for the two Elsasser number limits, $\Lambda = 0.1$ and $\Lambda = 10$ based on Earth’s core estimates of $Ek = 10^{-15}$ and $Pr = 0.1$, plotted as blue and red solid lines, respectively. The semi-transparent blue shading denotes the estimated N_c – Ra range for Earth’s core, while the black dash-dotted line marks the transition threshold $N_c = 3$. Most estimates fall above this threshold, placing Earth’s core in the magnetically damped regime, consistent with our experimental results.

Figure 11b presents Re_{MD} , as expressed via (23), as a function of the Rayleigh number Ra . The predictions are shown for two Elsasser numbers, $\Lambda = 0.1$ (blue solid line) and $\Lambda = 10$ (red solid line), using Earth’s core estimates of $Ek = 10^{-15}$ and $Pr = 0.1$. The semi-transparent blue region indicates estimated outer core ranges of $Ra \in [10^{23}, 10^{29}]$ and $\Lambda \in [0.1, 1]$ (identical to the blue region in Figure 1b). The light yellow rectangle represents the estimated range of Re in Earth’s core (e.g., Finlay and Amit, 2011; Holme, 2015; Livermore et al., 2017). The overlap of the blue and yellow shaded regions, edged in green, defines the range of Ra and Re_{MD} consistent with our laboratory experimental predictions. The center of the overlap region in Figure 11 corresponds to an Earth’s core Rayleigh number estimate of $Ra \approx 5 \times 10^{25}$, with the edges of the overlap region corresponding to Rayleigh values ranging from $Ra \approx 10^{24}$ to 5×10^{26} . These values are in good agreement with previous estimates (e.g., Gubbins, 2001).

The purple solid line in Figure 11b corresponds to Re_{df} scaling (13), which is close to $Re_{MD} = (2/\sqrt{3})Re_{df}$ (21) at $N_\ell = 3$ according to the best-fit obtained in Figure 10. This diffusion-free RC model for the convective flow velocities intersects the yellow shaded region between $Ra \approx 3 \times 10^{22}$ and 3×10^{24} . These DF branch predictions are still within the range of estimated core Ra , and, according to our extrapolations, likely constitute lower bounding Ra estimates for convection in Earth’s outer core. The Earth’s core-like range (semi-transparent blue region) lies mostly below Re_{df} , indicating a magnetically damped flow regime. This is consistent with Figure 11a, which shows that the predicted convective interaction parameter N_c for the Earth’s core remains largely above $N_c > 3$, where the flow is magnetically damped.

In making these Figure 11 estimates for Ra in Earth’s core, it must be pointed out that we are using large-scale core-mantle boundary flow inversion results as constraints on the small-scale convective flow within the bulk core. This may indeed be accurate and appropriate, but it is possible that the large-scale inferred surface velocities differ substantively from local convective-scale flows deep within the core (e.g., Holme, 2015; Holdenried-

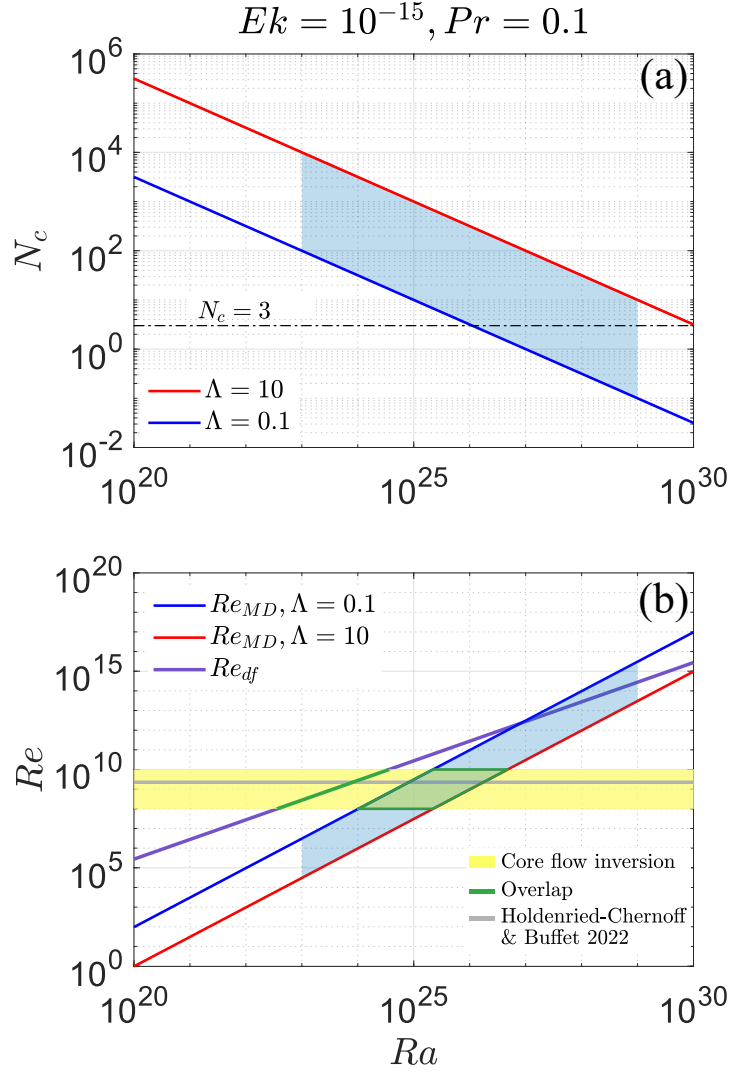


Figure 11: (a) Convective interaction parameter N_c via (8) and (b) magnetically damped Reynolds number Re_{MD} based on the predictions from (23) as a function Rayleigh number Ra , using Earth's outer core parameters: $Ek = 10^{-15}$, $Pr = 0.1$. Blue and red solid lines represent $\Lambda = 0.1$ and $\Lambda = 10$, respectively. The purple solid line marks the DF scaling Re_{df} . The semi-transparent blue region shows the estimated range of Ra - Λ in Earth's outer core corresponding to semi-transparent rectangle box shown in Figure 1b, the light yellow area indicates the corresponding estimated range of Re from Finlay and Amit (2011); Roberts and King (2013), the overlap of these estimations is marked by green solid line or green border lozenge, grey solid line from Holdenried-Chernoff and Buffett (2022).

Chernoff and Buffett, 2022; Oliver et al., 2023). To address this point, we include the grey horizontal line that denotes the turbulent diffusivity estimate from Holdenried-Chernoff and Buffett (2022) for bulk rms outer core velocity. This estimate agrees well with that of the velocity estimate from core flow inversion, and thus supports our Figure 11 predictions.

6. Conclusion

We have presented the results of a series of laboratory experiments in rotating magnetoconvection using liquid gallium to systematically explore the parameter regime characterized by moderate Ekman numbers and Elsasser numbers of order unity. Rotating convection cases were also investigated to provide a baseline for comparison with the RMC data. This study presents the first direct measurements of convective velocities in the $\Lambda = 1$, $Pr \ll 1$ magnetostrophic regime, a regime theoretically predicted to govern the local convection dynamics in planetary core settings (Aurnou and King, 2017; Teed and Dormy, 2025).

At $Ek = 10^{-4}$, the flow is not strongly influenced by the presence of an imposed $\Lambda = 1$ magnetic field. This is because inertial effects are equivalent to, or dominate, over both Coriolis and Lorentz forces in these $Ek = 10^{-4}$ experiments. In contrast, at $Ek = 10^{-5}$, inertial accelerations are subdominant, allowing the magnetic field to significantly alter the flow pattern, leading to larger-scale structures and reduced turbulence intensity.

Quantitatively, we find convective heat transfer and flow velocities in RMC cases exhibit a relatively sharp transition at a local interaction parameter $N_\ell \approx 3$. Above this threshold, the heat transfer is enhanced, which has been previously reported in both liquid metal experimental studies (King and Aurnou, 2015; Grannan et al., 2022), but has been interpreted to be due to the presence of magneto-wall modes or magnetostrophic bulk modes based only on sparse thermal field measurements. Here, we directly measure the suppression of bulk convective velocities in the $N_\ell \gtrsim 3$ regime is reported for the first time in liquid metal RMC experiments. These suppressed magnetostrophic convective velocities are accompanied by enhanced convective heat transfer. This enhancement may be explained by an increased coherence of the magneto-suppressed flow field, an argument that is qualitatively similar to that found in the constrained Rayleigh–Bénard convection literature (Huang et al., 2013; Chen et al., 2023). Below the $N_\ell \approx 3$ threshold, the measured velocities consistently scale with both the CIA and the diffusivity-

free RC predictions, indicating that the flow is in the geostrophic turbulent regime. In addition, the $N_\ell \approx 3$ transition found in our quasi-static liquid metal experiments is in basic agreement with the $N_\ell \approx 2$ dipolarity transition found in the spherical shell dynamo modeling study of Soderlund et al. (2025).

We derived a set of predictive formulations for the Reynolds number, (21) and (23), that depend solely on externally estimable parameters (Ra , Ek , Pr , Λ), enabling core velocity estimations to be made without direct measurements. Applying these experimental velocity scalings to estimate the convective Reynolds number in Earth’s outer core, our Re_{MD} -based predictions align well with previous geophysical estimates and suggest that convection in Earth’s outer core occurs at a Rayleigh number of $Ra \approx 5 \times 10^{25}$ and a convective Rossby number of $Ro_c \approx 2 \times 10^{-2}$, parameter values which are notoriously difficult to obtain for deep planetary core interiors.

Our experimental results also have implications for planetary dynamo models. Most $Ek \gtrsim 10^{-5}$ dynamo models are in the ‘weak field’ regime in which Lorentz forces are significantly smaller than Coriolis (e.g., Schaeffer et al., 2017). Even at the small, local scale of hydrodynamic RC onset, the local Elsasser number is typically below unity in these high Ek models (Aurnou and King, 2017). Our results imply that the velocities in such models should tend towards the diffusivity-free RC scaling, as this provides the upper bounding velocities when $N_\ell \lesssim 1$, as shown in Figure 9c. In contrast, when $Ek \lesssim 10^{-5}$, ‘strong field’ dynamo action tends to occur in which the local scale Elsasser number is order one or greater and the magnetic energy tends to swamp the kinetic energy (Yadav et al., 2016b; Schaeffer et al., 2017; Dormy, 2025). In these models, we expect locally magnetostrophic convective flows to be larger-scale and magnetically damped in their intensity, as found here in our $N_\ell \gtrsim 3$ cases. Since the vast majority of dynamo simulations to date have been carried out with $Ek \gtrsim 10^{-5}$, we predict that most will tend to track well with diffusivity-free rotating convective velocity scaling predictions (e.g., Aurnou et al., 2020; Hadjerci et al., 2024; Abbate et al., 2024).

7. Acknowledgement

We gratefully acknowledge funding for this project from the NSF Geophysics Program via EAR award #2143939.

Appendix A. Appendix

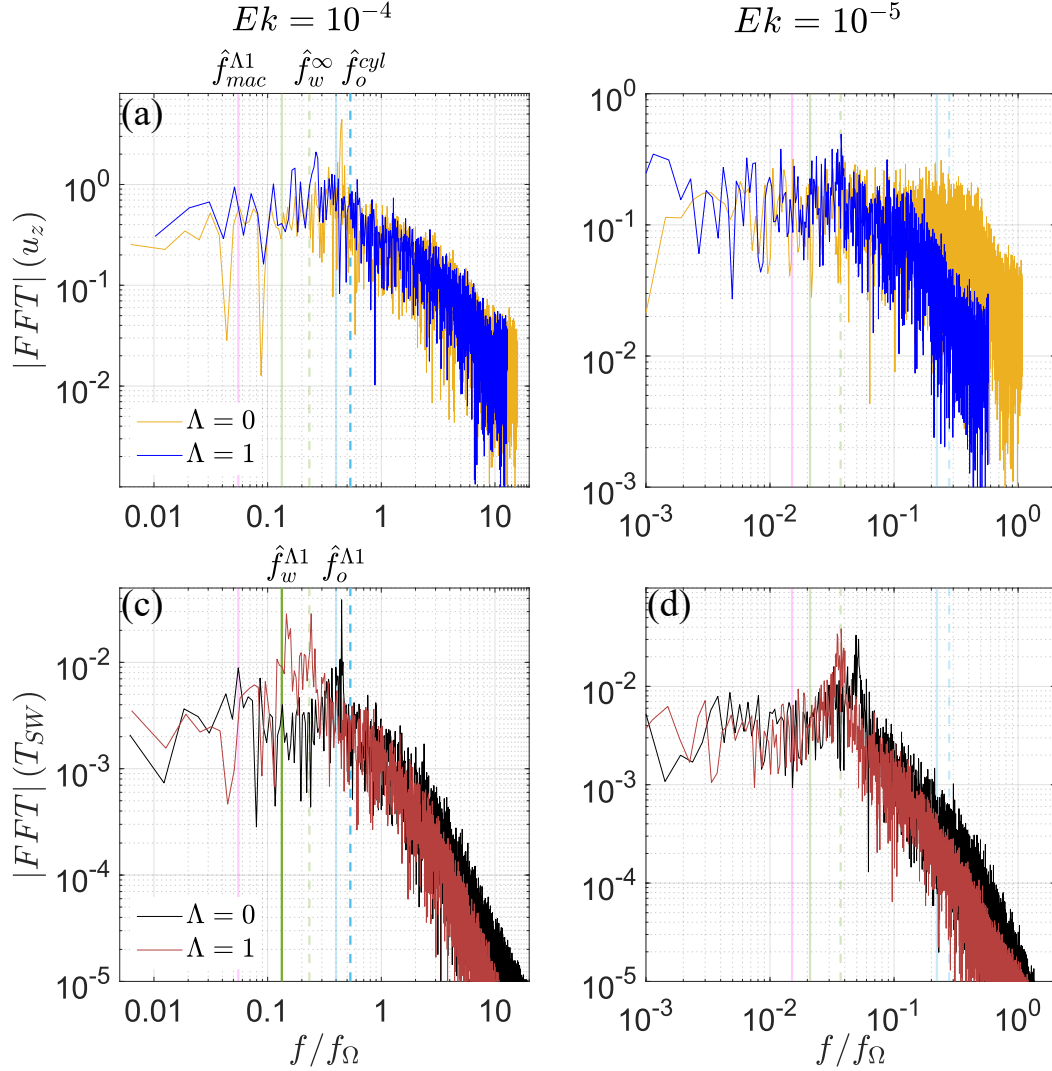


Figure A.12: Amplitude of the Fourier Transform of vertical velocity u_z : gold $\Lambda = 0$ and blue $\Lambda = 1$ and of side-wall temperature signal: black $\Lambda = 0$ and brick red $\Lambda = 1$ (a, c) $Ek = 10^{-4}$ and (b, d) $Ek = 10^{-5}$; the velocities data correspond to Figure 5; pink dashed line: mac frequency prediction $\hat{f}_{mac}^{\Lambda 1}$; green solid line: wall mode frequency prediction $\hat{f}_w^{\Lambda 1}$ with $\Lambda = 1$; green dashed line: wall mode frequency prediction \hat{f}_w^∞ with $\Lambda = 0$; light blue solid line: oscillatory mode frequency prediction $\hat{f}_o^{\Lambda 1}$ with $\Lambda = 1$; light blue dashed line: oscillatory mode frequency prediction \hat{f}_o^{cyl} with $\Lambda = 0$.

References

- Jewel A. Abbate. *Laboratory-Theoretical Investigations of Rotating Convection in Planetary Interiors*. PhD thesis, 2024.
- Jewel A. Abbate and Jonathan M. Aurnou. Rotating convective turbulence in moderate to high prandtl number fluids. *Geophysical & Astrophysical Fluid Dynamics*, 117(6):397–436, 2023. doi: 10.1080/03091929.2023.2280874.
- Jewel A Abbate and Jonathan M Aurnou. Shadowgraph measurements of rotating convective planetary core-style flows. *Journal of Geophysical Research: Planets*, 129(9):e2024JE008471, 2024.
- Jewel A. Abbate, Yufan Xu, Tobias Vogt, Susanne Horn, Keith Julien, and Jonathan M. Aurnou. Diffusivity-free turbulence in tabletop rotating rayleigh-bénard convection experiments. 2024.
- Julien Aubert, Daniel Brito, Henri-Claude Nataf, Philippe Cardin, and Jean-Paul Masson. A systematic experimental study of rapidly rotating spherical convection in water and liquid gallium. *Physics of the Earth and Planetary Interiors*, 128(1):51–74, 2001. ISSN 0031-9201. doi: [https://doi.org/10.1016/S0031-9201\(01\)00277-1](https://doi.org/10.1016/S0031-9201(01)00277-1). Dynamics and Magnetic Fields of the Earth’s and Planetary Interiors.
- Kélig Aujogue, Alban Pothérat, and Binod Sreenivasan. Onset of plane layer magnetoconvection at low ekman number. *Physics of Fluids*, 27(10), 2015.
- Jonathan Aurnou, Steven Andreadis, Lixin Zhu, and Peter Olson. Experiments on convection in earth’s core tangent cylinder. *Earth and Planetary Science Letters*, 212(1):119–134, 2003. ISSN 0012-821X. doi: [https://doi.org/10.1016/S0012-821X\(03\)00237-1](https://doi.org/10.1016/S0012-821X(03)00237-1).
- Jonathan M. Aurnou and Eric M. King. The cross-over to magnetostrophic convection in planetary dynamo systems. *Proceedings of the Royal Society A: Mathematical, Physical and Engineering Sciences*, 473(2199):20160731, 2017.
- Jonathan M. Aurnou, Michael A. Calkins, Jonathan S. Cheng, Keith Julien, Eric M. King, David Nieves, Krista M. Soderlund, and Stephan Stellmach. Rotating convective turbulence in earth and planetary cores. *Physics of the Earth and Planetary Interiors*, 246:52–71, 2015.

- Jonathan M Aurnou, Vincent Bertin, Alexander M Grannan, Susanne Horn, and Tobias Vogt. Rotating thermal convection in liquid gallium: multi-modal flow, absent steady columns. *Journal of Fluid Mechanics*, 846: 846–876, 2018.
- Jonathan M. Aurnou, Susanne Horn, and Keith Julien. Connections between nonrotating, slowly rotating, and rapidly rotating turbulent convection transport scalings. *Phys. Rev. Res.*, 2:043115, Oct 2020. doi: 10.1103/PhysRevResearch.2.043115.
- Adrian J Barker, Adam M Dempsey, and Yoram Lithwick. Theory and simulations of rotating convection. *The Astrophysical Journal*, 791(1):13, 2014.
- Vincent Bouillaut, Benjamin Miquel, Keith Julien, Sébastien Aumaître, and Basile Gallet. Experimental observation of the geostrophic turbulence regime of rapidly rotating convection. *Proceedings of the National Academy of Sciences*, 118(44):e2105015118, 2021. doi: 10.1073/pnas.2105015118.
- Daniel Brito, Henri-Claude Nataf, Philippe Cardin, Julien Aubert, and Jean-Paul Masson. Ultrasonic doppler velocimetry in liquid gallium. *Experiments in fluids*, 31(6):653–663, 2001.
- Daniel Brito, Jonathan Aurnou, and Philippe Cardin. Turbulent viscosity measurements relevant to planetary core-mantle dynamics. *Physics of the Earth and Planetary Interiors*, 141(1):3–8, 2004.
- Michael A Calkins, Keith Julien, Steven M Tobias, and Jonathan M Aurnou. A multiscale dynamo model driven by quasi-geostrophic convection. *Journal of Fluid Mechanics*, 780:143–166, 2015.
- Maria E Camisassa and Nicholas A Featherstone. Solar-like to antisolar differential rotation: a geometric interpretation. *The Astrophysical Journal*, 938(1):65, 2022.
- Philippe Cardin and Peter Olson. Chaotic thermal convection in a rapidly rotating spherical shell: consequences for flow in the outer core. *Physics of the Earth and Planetary Interiors*, 82(3):235–259, 1994. ISSN 0031-9201. doi: [https://doi.org/10.1016/0031-9201\(94\)90075-2](https://doi.org/10.1016/0031-9201(94)90075-2).

- Subrahmanyan Chandrasekhar. *Hydrodynamic and Hydromagnetic Stability*. Clarendon Press, 1961.
- Subrahmanyan Chandrasekhar and Donna D. : Elbert. The instability of a layer of fluid heated below and subject to coriolis forces. ii. *Proceedings of the Royal Society of London. Series A. Mathematical and Physical Sciences*, 231(1185):198–210, 1955. doi: 10.1098/rspa.1955.0166.
- Xin-Yuan Chen, Yi-Chao Xie, Juan-Cheng Yang, and Ming-Jiu Ni. Strong coupling of flow structure and heat transport in liquid metal thermal convection. *Journal of Fluid Mechanics*, 975:A21, 2023.
- Jonathan S Cheng, Jonathan M Aurnou, Keith Julien, and Rudie PJ Kunen. A heuristic framework for next-generation models of geostrophic convective turbulence. *Geophysical & Astrophysical Fluid Dynamics*, 112(4): 277–300, 2018.
- Jonathan S. Cheng, Ibrahim Mohammad, Bitong Wang, Declan F. Keogh, Jarod M. Forer, and Douglas H. Kelley. Oscillations of the large-scale circulation in experimental liquid metal convection at aspect ratios 1.4–3. *Journal of Fluid Mechanics*, 949:A42, 2022. doi: 10.1017/jfm.2022.778.
- Kai Leong Chong, Yantao Yang, Shi-Di Huang, Jin-Qiang Zhong, Richard JAM Stevens, Roberto Verzicco, Detlef Lohse, and Ke-Qing Xia. Confined rayleigh-bénard, rotating rayleigh-bénard, and double diffusive convection: A unifying view on turbulent transport enhancement through coherent structure manipulation. *Physical review letters*, 119(6):064501, 2017.
- Emmanuel Dormy. Strong-field spherical dynamos. *Journal of Fluid Mechanics*, 789:500–513, 2016.
- Emmanuel Dormy. Rapidly rotating magnetohydrodynamics and the geodynamo. *Annual Review of Fluid Mechanics*, 57, 2025.
- Ibrahim A. Eltayeb and Subrahmanyan Chandrasekhar. Hydromagnetic convection in a rapidly rotating fluid layer. *Proceedings of the Royal Society of London. A. Mathematical and Physical Sciences*, 326(1565):229–254, 1972. doi: 10.1098/rspa.1972.0007.

- Christopher C. Finlay and Hagay Amit. On flow magnitude and field-flow alignment at earth’s core surface. *Geophysical Journal International*, 186(1):175–192, 07 2011. ISSN 0956-540X. doi: 10.1111/j.1365-246X.2011.05032.x.
- Thomas Gastine, Johannes Wicht, and Jonathan M. Aurnou. Zonal flow regimes in rotating anelastic spherical shells: An application to giant planets. *Icarus*, 225(1):156–172, 2013a.
- Thomas Gastine, Rakesh K Yadav, Julien Morin, Ansgar Reiners, and Johannes Wicht. From solar-like to antisolar differential rotation in cool stars. *Monthly Notices of the Royal Astronomical Society: Letters*, 438(1): L76–L80, 2013b.
- Nicolas Gillet, Dominique Jault, Elisabeth Canet, and Alexandre Fournier. Fast torsional waves and strong magnetic field within the earth’s core. *Nature*, 465(7294):74–77, 2010. ISSN 1476-4687. doi: 10.1038/nature09010.
- H. F. Goldstein, E. Knobloch, I. Mercader, and M. Net. Convection in a rotating cylinder. part 2. linear theory for low prandtl numbers. *Journal of Fluid Mechanics*, 262:293–324, 1994. doi: 10.1017/S0022112094000510.
- David Goluskin. *Internally heated convection and Rayleigh–Bénard convection*. Springer, 2016.
- Alexander M. Grannan, Jonathan S. Cheng, Ashna Aggarwal, Emily K. Hawkins, Yufan Xu, Susanne Horn, Jose Sánchez-Álvarez, and Jonathan M. Aurnou. Experimental pub crawl from rayleigh–bénard to magnetostrophic convection. *Journal of Fluid Mechanics*, 939:R1, 2022. doi: 10.1017/jfm.2022.204.
- Harvey P. Greenspan. *Theory of Rotating Fluids*. Cambridge University Press, 1969.
- David Gubbins. The rayleigh number for convection in the earth’s core. *Physics of the Earth and Planetary Interiors*, 128(1):3–12, 2001. ISSN 0031-9201. doi: [https://doi.org/10.1016/S0031-9201\(01\)00273-4](https://doi.org/10.1016/S0031-9201(01)00273-4). Dynamics and Magnetic Fields of the Earth’s and Planetary Interiors.

- Céline Guervilly, Philippe Cardin, and Nathanaël Schaeffer. Turbulent convective length scale in planetary cores. *Nature*, 570:368–371, 2019. doi: 10.1038/s41586-019-1301-5.
- Gabriel Hadjerci, Vincent Bouillaut, Benjamin Miquel, and Basile Gallet. Rapidly rotating radiatively driven convection: experimental and numerical validation of the ‘geostrophic turbulence’ scaling predictions. *Journal of Fluid Mechanics*, 998:A9, 2024. doi: 10.1017/jfm.2024.556.
- Emily K. Hawkins, Jonathan S. Cheng, Jewel A. Abbate, Timothy Pilegard, Stephan Stellmach, Keith Julien, and Jonathan M. Aurnou. Laboratory models of planetary core-style convective turbulence. *Fluids*, 8(4), 2023. ISSN 2311-5521. doi: 10.3390/fluids8040106.
- J. Herrmann and Friedrich Hermann Busse. Asymptotic theory of wall-attached convection in a rotating fluid layer. *Journal of Fluid Mechanics*, 255:183–194, 1993. doi: 10.1017/S0022112093002447.
- D Holdenried-Chernoff and B_A Buffett. Evidence for turbulent magnetic diffusion in earth’s core. *Geochemistry, Geophysics, Geosystems*, 23(12):e2022GC010672, 2022.
- Richard Holme. Large-scale flow in the core. In Gerald Schubert, editor, *Treatise on Geophysics, 2nd edition*, volume 8, pages 107–130. Elsevier, 2015.
- Susanne Horn and Jonathan M. Aurnou. The elbert range of magnetostrophic convection. i. linear theory. *Proceedings of the Royal Society A: Mathematical, Physical and Engineering Sciences*, 478(2264):20220313, 2022. doi: 10.1098/rspa.2022.0313.
- Susanne Horn and Jonathan M. Aurnou. The elbert range of magnetostrophic convection. ii. comparing linear theory to nonlinear low- Pr_m simulations. *Proceedings of the Royal Society A: Mathematical, Physical and Engineering Sciences*, 481(2310):20240016, 2025. doi: 10.1098/rspa.2024.0016.
- Susanne Horn and Peter J. Schmid. Prograde, retrograde, and oscillatory modes in rotating rayleigh–bénard convection. *Journal of Fluid Mechanics*, 831:182–211, 2017. doi: 10.1017/jfm.2017.631.

- Susanne Horn, Peter J Schmid, and Jonathan M Aurnou. Unravelling the large-scale circulation modes in turbulent rayleigh-bénard convection (a). *Europhysics Letters*, 136(1):14003, 2022.
- Shi-Di Huang, Matthias Kaczorowski, Rui Ni, and Ke-Qing Xia. Confinement-induced heat-transport enhancement in turbulent thermal convection. *Phys. Rev. Lett.*, 111:104501, Sep 2013.
- Andrew P Ingersoll and David Pollard. Motion in the interiors and atmospheres of jupiter and saturn: Scale analysis, anelastic equations, barotropic stability criterion. *Icarus*, 52(1):62–80, 1982.
- Chris A. Jones. Planetary magnetic fields and fluid dynamos. *Annual Review of Fluid Mechanics*, 43:583–614, 2011. ISSN 1545-4479. doi: <https://doi.org/10.1146/annurev-fluid-122109-160727>.
- Keith Julien and Edgar Knobloch. Strongly nonlinear convection cells in a rapidly rotating fluid layer: the tilted f-plane. *Journal of Fluid Mechanics*, 360:141–178, 1998. doi: 10.1017/S0022112097008446.
- Keith Julien, Edgar Knobloch, and Joseph Werne. *Reduced equations for rotationally constrained convection. In Turbulence and Shear Flows, I*. Begell House, 1999.
- Keith Julien, Edgar Knobloch, Antonio M. Rubio, and Geoffrey M. Vasil. Heat transport in low-rossby-number rayleigh-bénard convection. *Phys. Rev. Lett.*, 109:254503, Dec 2012a. doi: 10.1103/PhysRevLett.109.254503.
- Keith Julien, Antonio M Rubio, Ian Grooms, and Edgar Knobloch. Statistical and physical balances in low rossby number rayleigh-bénard convection. *Geophysical & Astrophysical Fluid Dynamics*, 106(4-5):392–428, 2012b.
- Eric M. King and Jonathan M. Aurnou. Magnetostrophic balance as the optimal state for turbulent magnetoconvection. *Proceedings of the National Academy of Sciences*, 112(4):990–994, 2015. doi: 10.1073/pnas.1417741112.
- Eric M. King and Bruce A. Buffett. Flow speeds and length scales in geodynamo models: The role of viscosity. *Earth and Planetary Science Letters*, 371:156–162, June 2013. doi: <https://doi.org/10.1016/j.epsl.2013.04.001>.

- Eric M King, Stephan Stellmach, and Jonathan M Aurnou. Heat transfer by rapidly rotating rayleigh–bénard convection. *Journal of Fluid Mechanics*, 691:568–582, 2012.
- Rudie P. J. Kunnen. The geostrophic regime of rapidly rotating turbulent convection. *Journal of Turbulence*, 22(4-5):267–296, 2021. doi: 10.1080/14685248.2021.1876877.
- Simon Lepot, Sébastien Aumaître, and Basile Gallet. Radiative heating achieves the ultimate regime of thermal convection. *Proceedings of the National Academy of Sciences*, 115(36):8937–8941, 2018. doi: 10.1073/pnas.1806823115.
- X. Liao, K. Zhang, and Y. Chang. On boundary-layer convection in a rotating fluid layer. *Journal of Fluid Mechanics*, 549:375–384, 2006. doi: 10.1017/S0022112005008189.
- Philip W Livermore, Rainer Hollerbach, and Christopher C Finlay. An accelerating high-latitude jet in earth’s core. *Nature Geoscience*, 10(1):62–68, 2017.
- Jun Mabuchi, Youhei Masada, and Akira Kageyama. Differential rotation in magnetized and non-magnetized stars. *The Astrophysical Journal*, 806(1): 10, 2015.
- Pearn P. Nüiler and Frederic E. Bisshopp. On the influence of coriolis force on onset of thermal convection. *Journal of Fluid Mechanics*, 22(4):753–761, 1965. doi: 10.1017/S002211206500112X.
- Jérôme Noir, Daniel Brito, Keith Aldridge, and Philippe Cardin. Experimental evidence of inertial waves in a precessing spheroidal cavity. *Geophysical Research Letters*, 28(19):3785–3788, 2001.
- Tobias G Oliver, Adrienne S Jacobi, Keith Julien, and Michael A Calkins. Small scale quasigeostrophic convective turbulence at large rayleigh number. *Physical Review Fluids*, 8(9):093502, 2023.
- Joseph Proudman and Horace Lamb. On the motion of solids in a liquid possessing vorticity. *Proceedings of the Royal Society of London. Series A, Containing Papers of a Mathematical and Physical Character*, 92(642): 408–424, 1916. doi: 10.1098/rspa.1916.0026.

- Paul H Roberts and Eric M King. On the genesis of the earth’s magnetism. *Reports on Progress in Physics*, 76(9):096801, sep 2013. doi: 10.1088/0034-4885/76/9/096801.
- Ataru Sakuraba. Linear magnetoconvection in rotating fluid spheres permeated by a uniform axial magnetic field. *Geophysical & Astrophysical Fluid Dynamics*, 96(4):291–318, 2002.
- Nathanaël Schaeffer, Dominique Jault, H-C Nataf, and Alexandre Fournier. Turbulent geodynamo simulations: a leap towards earth’s core. *Geophysical Journal International*, 211(1):1–29, 2017.
- Krista M Soderlund, Andrey Sheyko, Eric M King, and Jonathan M Aurnou. The competition between lorentz and coriolis forces in planetary dynamos. *Progress in Earth and Planetary Science*, 2(1):24, 2015.
- Krista M Soderlund, Paula Wulff, Petri J Käpylä, and Jonathan M Aurnou. Magnetohydrodynamic control of differential rotation and dynamo transitions: rise of the local magnetic rossby number. *Monthly Notices of the Royal Astronomical Society*, 541(2):1816–1830, 07 2025. ISSN 0035-8711. doi: 10.1093/mnras/staf1081.
- Edward A Spiegel. Convection in stars: I. basic boussinesq convection. *Annual Review of Astronomy and Astrophysics*, vol. 9, p. 323, 9:323, 1971.
- David J Stevenson. Turbulent thermal convection in the presence of rotation and a magnetic field: a heuristic theory. *Geophysical & Astrophysical Fluid Dynamics*, 12(1):139–169, 1979.
- Yasushi Takeda. Velocity profile measurement by ultrasonic doppler method. *Experimental Thermal and Fluid Science*, 10(4):444–453, 1995. ISSN 0894-1777. doi: [https://doi.org/10.1016/0894-1777\(94\)00124-Q](https://doi.org/10.1016/0894-1777(94)00124-Q). Experimental methods in Thermal and Fluid Science.
- Geoffrey Ingram Taylor and Horace Lamb. Motion of solids in fluids when the flow is not irrotational. *Proceedings of the Royal Society of London. Series A, Containing Papers of a Mathematical and Physical Character*, 93(648):99–113, 1917. doi: 10.1098/rspa.1917.0007.
- Robert J Teed and Emmanuel Dormy. Scaling of strong-field spherical dynamos. *arXiv preprint arXiv:2508.05639*, 2025.

- Adrian van Kan, Keith Julien, Benjamin Miquel, and Edgar Knobloch. Bridging the rossby number gap in rapidly rotating thermal convection. *Journal of Fluid Mechanics*, 1010:A42, 2025.
- Geoffrey M. Vasil, Keaton J. Burns, Daniel Lecoanet, Jeffrey S. Oishi, Benjamin P. Brown, and Keith Julien. Rapidly rotating wall-mode convection. *arXiv preprint arXiv:2409.20541*, 2024. doi: 10.48550/arXiv.2409.20541.
- Tobias Vogt, Susanne Horn, Alexander M. Grannan, and Jonathan M. Aurnou. Jump rope vortex in liquid metal convection. *Proceedings of the National Academy of Sciences*, 115(50):12674–12679, 2018. doi: 10.1073/pnas.1812260115.
- Tobias Vogt, Susanne Horn, and Jonathan M. Aurnou. Oscillatory thermal-inertial flows in liquid metal rotating convection. *Journal of Fluid Mechanics*, 911:A5, 2021a. doi: 10.1017/jfm.2020.976.
- Tobias Vogt, Juan-Cheng Yang, Felix Schindler, and Sven Eckert. Free-fall velocities and heat transport enhancement in liquid metal magnetoconvection. *Journal of Fluid Mechanics*, 915:A68, 2021b.
- Stephan Weiss and Guenter Ahlers. Heat transport by turbulent rotating rayleigh-bénard convection and its dependence on the aspect ratio. *Journal of fluid mechanics*, 684:407–426, 2011.
- Ke-Qing Xia, Shi-Di Huang, Yi-Chao Xie, and Lu Zhang. Tuning heat transport via coherent structure manipulation: recent advances in thermal turbulence. *National Science Review*, 10(6):nwad012, 2023.
- Yufan Xu, Jewel Abbate, Cy David, Tobias Vogt, and Jonathan Aurnou. Thermovelocity characterization of liquid metal convection in a rotating slender cylinder. *International Journal of Heat and Mass Transfer*, 252:127325, 2025.
- Rakesh K Yadav, Thomas Gastine, Ulrich R Christensen, Lucia DV Duarte, and Ansgar Reiners. Effect of shear and magnetic field on the heat-transfer efficiency of convection in rotating spherical shells. *Geophysical Journal International*, 204(2):1120–1133, 2016a.
- Rakesh K. Yadav, Thomas Gastine, Ulrich R. Christensen, Scott J. Wolk, and Katja Poppenhaeger. Approaching a realistic force balance in geodynamo

- simulations. *Proceedings of the National Academy of Sciences*, 113(43): 12065–12070, 2016b. doi: 10.1073/pnas.1608998113.
- Ming Yan, Michael A. Calkins, Stefano Maffei, Keith Julien, Steven M. Tobias, and Philippe Marti. Heat transfer and flow regimes in quasi-static magnetoconvection with a vertical magnetic field. *Journal of Fluid Mechanics*, 877:1186–1206, 2019. doi: 10.1017/jfm.2019.615.
- Keke Zhang and Xinhao Liao. The onset of convection in rotating circular cylinders with experimental boundary conditions. *Journal of Fluid Mechanics*, 622:63–73, 2009. doi: 10.1017/S002211200800517X.
- Fang Zhong, Robert Ecke, and Victor Steinberg. Rotating rayleigh-bénard convection: Küppers-lortz transition. *Physica D: Nonlinear Phenomena*, 51(1):596–607, 1991. ISSN 0167-2789. doi: [https://doi.org/10.1016/0167-2789\(91\)90266-C](https://doi.org/10.1016/0167-2789(91)90266-C).
- Till Zürner, Felix Schindler, Tobias Vogt, Sven Eckert, and Jörg Schumacher. Combined measurement of velocity and temperature in liquid metal convection. *Journal of Fluid Mechanics*, 876:1108–1128, 2019. doi: 10.1017/jfm.2019.556.

Appendix A. Appendix

Λ	$Ek \cdot 10^4$	$Ra \cdot 10^{-6}$	\widetilde{Ra}_o^∞	\widetilde{Ra}_o^{cyl}	\widetilde{Ra}_w^∞	$\widetilde{Ra}_{mac}^\infty$	\widetilde{Ra}_s^∞	Pr	$P(W)$	ΔT	Nu	$Re_{z,rms}$	Ro_c
0	1	0.335	10.55	3.39	1.40	—	0.18	0.0275	20	1.33	1.44	265	0.345
0	1	0.615	19.37	6.22	2.57	—	0.32	0.0275	50	2.44	2.03	534	0.467
0	1	0.783	24.67	7.92	3.27	—	0.41	0.0275	80	3.08	2.57	911	0.525
0	1	3.08	97.03	31.15	12.88	—	1.62	0.0275	780	12.01	6.69	2566	1.04
1	1	0.329	1.17	—	1.41	0.58	0.19	0.0275	20	1.31	1.48	—	0.342
1	1	0.600	2.14	—	2.58	1.05	0.34	0.0275	50	2.37	2.09	—	0.461
1	1	0.785	2.80	—	3.37	1.37	0.44	0.0272	80	3.08	2.62	326	0.526
1	1	1.17	4.17	—	5.02	2.05	0.66	0.0273	150	4.61	3.3	603	0.643
1	1	1.41	5.02	—	6.05	2.47	0.79	0.0273	200	5.56	3.69	864	0.706
1	1	1.63	5.81	—	7.00	2.85	0.92	0.0272	250	6.40	4.02	1065	0.758
1	1	1.85	6.59	—	7.94	3.24	1.04	0.0271	300	7.21	4.3	1202	0.804
1	1	2.04	7.27	—	8.76	3.57	1.15	0.0270	350	7.96	4.55	1340	0.845
1	1	2.24	7.98	—	9.62	3.92	1.26	0.0269	400	8.69	4.74	1430	0.883
1	1	2.44	8.69	—	10.48	4.27	1.37	0.0268	450	9.43	4.94	1532	0.92
1	1	2.62	9.33	—	11.25	4.58	1.47	0.0267	500	10.12	5.13	1484	0.963
1	1	2.80	9.97	—	12.02	4.90	1.58	0.0267	550	10.77	5.28	1629	0.983
1	1	2.98	10.62	—	12.79	5.21	1.68	0.0266	600	11.45	5.45	1743	1.01
1	1	3.13	11.15	—	13.44	5.47	1.76	0.0265	650	11.99	5.63	1849	1.04
1	1	3.31	11.79	—	14.21	5.79	1.86	0.0264	700	12.65	5.76	1933	1.07
1	1	3.57	12.72	—	15.33	6.24	2.01	0.0264	780	13.61	5.96	2005	1.1

Table A.3: Data table for the $Ek = 10^{-4}$ experiments.

Λ	$Ek \cdot 10^4$	$Ra \cdot 10^{-6}$	\widetilde{Ra}_o^∞	\widetilde{Ra}_o^{cyl}	\widetilde{Ra}_w^∞	$\widetilde{Ra}_{mac}^\infty$	\widetilde{Ra}_s^∞	Pr	$P(W)$	ΔT	Nu	$Re_{z,rms}$	Ro_c
0	0.4	0.441	4.40	1.52	0.64	—	0.07	0.0275	20	1.75	1.09	—	0.159
0	0.4	1.49	14.87	5.15	2.15	—	0.23	0.0272	100	5.86	1.71	492	0.290
0	0.4	1.93	19.26	6.67	2.78	—	0.30	0.0270	150	7.54	2.00	835	0.330
0	0.4	2.26	22.56	7.81	3.26	—	0.35	0.0270	200	8.82	2.31	766	0.357
0	0.4	5.02	50.10	17.34	7.24	—	0.78	0.0261	780	18.95	4.27	1786	0.523
1	0.4	0.441	0.60	—	0.73	0.31	0.07	0.0275	20	1.75	1.09	216	0.159
1	0.4	1.36	1.84	—	2.26	0.95	0.22	0.0272	100	5.33	1.88	517	0.277
1	0.4	1.74	2.36	—	2.89	1.22	0.28	0.0271	150	6.79	2.22	726	0.313
1	0.4	2.06	2.79	—	3.43	1.44	0.34	0.0271	200	8.05	2.54	977	0.341
1	0.4	2.59	3.51	—	4.31	1.82	0.42	0.0269	300	10.08	3.06	1072	0.381
1	0.4	2.86	3.87	—	4.76	2.01	0.47	0.0267	350	11.05	3.26	1139	0.399
1	0.4	3.08	4.17	—	5.12	2.16	0.50	0.0268	400	11.91	3.35	1243	0.414
1	0.4	3.33	4.51	—	5.54	2.34	0.54	0.0266	450	12.79	3.63	1274	0.429
1	0.4	3.55	4.81	—	5.91	2.49	0.58	0.0266	500	13.62	3.80	1351	0.443
1	0.4	3.78	5.12	—	6.29	2.65	0.62	0.0264	550	14.43	3.93	1401	0.456
1	0.4	4.00	5.42	—	6.65	2.81	0.65	0.0263	600	15.21	4.10	1429	0.468
1	0.4	4.39	5.94	—	7.30	3.08	0.72	0.0262	700	16.63	4.37	1553	0.490
1	0.4	4.67	6.32	—	7.77	3.27	0.76	0.0262	780	17.64	4.58	1596	0.504

Table A.4: Data table for the $Ek = 4 \times 10^{-5}$ experiments.

Λ	$Ek \cdot 10^4$	$Ra \cdot 10^{-6}$	\widetilde{Ra}_o^∞	\widetilde{Ra}_o^{cyl}	\widetilde{Ra}_w^∞	$\widetilde{Ra}_{mac}^\infty$	\widetilde{Ra}_s^∞	Pr	$P(W)$	ΔT	Nu	$Re_{z,rms}$	Ro_c
0	0.2	0.949	3.88	1.43	0.64	—	0.06	0.0273	40	3.74	1.03	325	0.124
0	0.2	1.97	8.05	2.97	1.33	—	0.12	0.0271	100	7.71	1.29	589	0.177
0	0.2	2.63	10.74	3.97	1.77	—	0.16	0.0269	150	10.21	1.46	746	0.204
0	0.2	6.89	28.15	10.40	4.65	—	0.43	0.0259	780	25.85	3.11	1580	0.305
1	0.2	0.968	0.63	—	0.79	0.34	0.06	0.0273	40	3.81	1.01	—	0.125
1	0.2	1.73	1.12	—	1.42	0.60	0.11	0.0271	100	6.76	1.48	—	0.166
1	0.2	2.32	1.51	—	1.90	0.81	0.15	0.0270	150	9.01	1.67	—	0.192
1	0.2	2.83	1.84	—	2.32	0.99	0.18	0.0267	200	10.91	1.86	212	0.211
1	0.2	3.33	2.16	—	2.72	1.16	0.21	0.0266	250	12.66	2.01	446	0.227
1	0.2	3.68	2.39	—	3.01	1.28	0.24	0.0266	300	14.12	2.18	561	0.240
1	0.2	4.03	2.62	—	3.30	1.40	0.26	0.0266	350	15.47	2.32	690	0.251
1	0.2	4.31	2.80	—	3.53	1.50	0.28	0.0266	400	16.56	2.47	783	0.260
1	0.2	4.66	3.03	—	3.81	1.62	0.30	0.0266	450	17.91	2.58	864	0.270
1	0.2	4.95	3.22	—	4.05	1.73	0.32	0.0265	500	18.94	2.73	969	0.278
1	0.2	5.17	3.36	—	4.23	1.80	0.33	0.0264	550	19.75	2.86	1014	0.284
1	0.2	5.53	3.59	—	4.52	1.93	0.36	0.0264	600	21.11	2.95	1113	0.294
1	0.2	5.86	3.81	—	4.79	2.04	0.38	0.0264	680	22.33	3.14	1185	0.302
1	0.2	6.32	4.11	—	5.17	2.20	0.41	0.0262	780	23.98	3.36	1327	0.313

Table A.5: Data table for the $Ek = 2 \times 10^{-5}$ experiments.

Λ	$Ek \cdot 10^4$	$Ra \cdot 10^{-6}$	\widetilde{Ra}_o^∞	\widetilde{Ra}_o^{cyl}	\widetilde{Ra}_w^∞	$\widetilde{Ra}_{mac}^\infty$	\widetilde{Ra}_s^∞	Pr	$P(W)$	ΔT	Nu	$Re_{z,rms}$	Ro_c
0	0.1	1.23	2.03	0.80	0.40	—	0.03	0.0272	50	4.81	1.01	—	0.069
0	0.1	2.52	4.17	1.64	0.82	—	0.06	0.0268	100	9.76	1.07	—	0.099
0	0.1	4.17	6.89	2.71	1.35	—	0.10	0.0267	200	16.01	1.25	289	0.127
0	0.1	5.73	9.47	3.73	1.86	—	0.14	0.0263	300	21.76	1.40	530	0.148
0	0.1	10.10	16.69	6.57	3.28	—	0.25	0.0253	780	36.89	2.17	1289	0.192
1	0.1	1.25	0.38	—	0.51	0.22	0.03	0.0272	50	4.88	1.00	—	0.070
1	0.1	2.38	0.73	—	0.97	0.42	0.06	0.0268	100	9.21	1.07	—	0.096
1	0.1	3.59	1.10	—	1.46	0.63	0.09	0.0267	200	13.87	1.46	106	0.118
1	0.1	4.84	1.48	—	1.97	0.85	0.12	0.0265	300	18.49	1.65	194	0.136
1	0.1	7.02	2.14	—	2.85	1.23	0.18	0.0260	550	26.43	2.13	424	0.163
1	0.1	7.49	2.29	—	3.05	1.31	0.19	0.0259	600	28.03	2.20	501	0.168
1	0.1	7.86	2.40	—	3.20	1.37	0.20	0.0258	650	29.31	2.28	542	0.171
1	0.1	8.23	2.51	—	3.35	1.44	0.21	0.0257	700	30.57	2.36	590	0.175
1	0.1	8.80	2.69	—	3.58	1.54	0.22	0.0256	780	32.57	2.47	691	0.181

Table A.6: Data table for the $Ek = 10^{-5}$ experiments.